Recent developments of Fe-based metal-organic frameworks and their composites in photocatalytic applications: fundamentals, synthesis and challenges

Riyadh Ramadhan Ikreedeegh [a, b]

[a] *Department of Analysis and Quality Control, Sarir Oil Refinery, Arabian Gulf Oil Company, El Kish, P.O. Box 263, Benghazi, Libya*
[b] *Chemical Reaction Engineering Group (CREG), School of Chemical and Energy Engineering, Universiti Teknologi Malaysia, 81310 UTM, Johor Bahru, Johor, Malaysia*

Nowadays, the use of efficient nanomaterials in the photocatalytic applications are highly demanded to maximize the utilization of solar light energy for sustainable fuel production and environmental remediation. Recently, there has been a growing research on the use of metal-organic framework (MOF) materials as photocatalysts owing to their unique structures and optoelectronic properties. Among these MOF materials, Fe-based MOF photocatalysts have attracted much attention in all fields of photocatalysis due to the presence of extensive iron−oxo (Fe−O) clusters which increase the visible light harvesting. Moreover, iron is considered as one of the low-cost and earth-abundant metals. In this mini-review, the recent developments in Fe-based MOF synthesis techniques with their major photocatalytic applications in oxygen production, hydrogen production, CO_2 reduction and pollutant photodegradation are summarized and deliberately explained. Finally, the main challenges regarding the Fe-based MOF photocatalysis with the future recommendations are addressed. The bibliography includes 175 references.

Contents

R.R.Ikreedeegh. Post-graduate student, Master in Chemical Engineering, Head of Department of Analysis and Quality Control, Sarir Oil Refinery, Arabian Gulf Oil Company (Benghazi, Libya), Member of the CREG at the School of Chemical and Energy Engineering, Universiti Teknologi Malaysia.
E-mail: riyadhkridiegh@gmail.com
Current research interests: renewable and clean energy sources, nano-materials including MOFs and TiO_2 nanotube composites for various photocatalytic applications (CO_2 reduction, H_2 production and CH_4 dry reforming).

1. Introduction

The ever-increasing consumption of fossil fuels has led to a serious global energy crisis due to high demands on these energy resources.[1] Moreover, burning of these fuels generates massive amounts of toxic pollutants including greenhouse gases (GHGs).[2, 3] On the other hand, solar energy is considered to be one of the best choices as an alternative and renewable energy resource due to its abundance and availability. Therefore, tremendous efforts were made to utilize solar light through various technologies. Among these solar light-driven technologies there is a photoreaction process known as photocatalysis. This process is conducted over the surface of a semiconductor material called a photocatalyst, when light having an equal or greater bandgap of that material is exposed to its surface, generates a huge population of electron−hole pairs (e^-/h^+), after which these photogenerated charge carriers undergo a series of reduction and oxidation (Redox) reactions to produce the final solar products.[4, 5]

In 1972, the first attempt of using TiO_2 as a photocatalyst was reported by Fujishima and Honda,[6] who highly promoted the field of solar energy applications. Many approaches were then designed using various semiconductor materials in all photocatalysis fields. These semiconductors include various nanostructured materials such as zeolites, zinc oxide (ZnO), zirconium oxide (ZrO_2), zinc sulfide (ZnS), magnesium oxide (MgO), graphitic carbon nitride ($g-C_3N_4$), perovskites and layered double hydroxides (LDHs).[7, 8] However, the performance of these materials is generally modest. Therefore, there is a significant need for the development

of more efficient photocatalytic materials for energy production and environmental remediation applications. According to previous studies, metal oxide photocatalysts such as TiO_2 have shown good photocatalytic performance under UV light. Unfortunately, the UV light represents only 3% of the solar light energy compared to 43% that of the visible light.[9,10] At the same time, the noble metal nanoparticles such as Pt, Au and Ag demonstrated great response to visible light and hence were applied to solve this issue. However, their high cost and low stability greatly limit their use in this field.[11,12]

Recently, new crystalline and low-cost materials known as metal-organic frameworks have been introduced to this field. These MOF materials have many advantages including high specific surface area, high porosity, well-ordered structures, visible light response and exceptional photocatalytic functionalities.[13–16] Among the most commonly studied MOFs, Fe-MOFs have been extensively investigated for many photocatalytic applications such as oxygen and hydrogen production, CO_2 reduction and photodegradation of pollutants.[17–19]

Iron is considered as a low toxic and inexpensive element due to its abundance in the earth's crust.[20] In comparison with the oxo-clusters in Zr- and Ti-containing MOFs, the $Fe-O$ clusters in Fe-MOFs can be directly excited by visible light irradiation making it an excellent visible-light-responsive material. Moreover, the Fe-MOFs has a bandgap ranging from 1.88 to 2.88 eV, which increases its photocatalytic activity under visible light, compared to wide bandgap energies exhibited by other types of MOFs such as MOF-5 (3.4 eV), MIL-125(Ti) (3.6 eV) and UiO-66(Zr) (3.9 eV).[21–23] All the above-mentioned merits of Fe-containing MOFs, in particular, make them promising photocatalysts and good competitors with other materials for energy production and environmental remediation applications.

Recently, Joseph *et al.*[24] reported the current advances in the applications of Fe-MOFs in wastewater treatment and presented a detailed discussion on the structural instabilities of these materials which limits their utilization in this field. However, the use of Fe-based MOF photocatalysts involves a wider range of applications that need to be presented. In 2017, Wang and Li[25] investigated Fe-MOFs as photocatalysts in various types of photocatalytic reactions with more focus on their visible light-harvesting properties. However, since then there have been many research studies that need to be summarized in a comprehensive review. Therefore, this review aims to summarize the recent studies reported over the past decade on the use of Fe-MOFs and their composites in the main photocatalytic applications.

This review provides a brief insight into the photocatalytic fundamentals of metal-organic framework materials and their classifications. Then, the recent developments of the main synthesis techniques used for the preparation of Fe-MOFs with the perspectives for industrial scale-up production are discussed in depth. Furthermore, the major photocatalytic applications of various Fe-MOFs in oxygen and hydrogen production, CO_2 reduction and pollutant photodegradation are summarized and deliberately explained. Finally, this review is concluded with the future recommendations and challenges associated with the applicability of Fe-MOF photocatalysts for energy production and environmental remediation applications.

2. Recent developments of Fe-based MOF materials

2.1. Development of MOFs in photocatalysis

In recent years, a new type of promising materials known as metal-organic frameworks has attracted researcher's interests mainly due to their excellent optoelectronic properties, ordered crystalline structures, tunable porosity and high mechanical and thermal stability. In catalysis, MOFs are considered as good materials, in which the partially-occupied metal sites can provide active sites act as Lewis acidic sites for both gas- and liquid-phase reactions.[26] Therefore, MOFs can catalyze a wide range of reactions including cycloaddition of CO_2 and epoxides,[27] cyanosilylation of aldehydes,[28] Friedel–Crafts reaction,[29] various organic processes[30] and isomerization reactions.[31] Moreover, stable MOFs can also be modified as redox catalysts by metalo-functionalization of their organic linkers. However, when MOFs were synthesized for the first time, they were studied mainly for gas storage and separation.[32–34] Later, they were extensively investigated for other uses including photocatalytic applications such as oxygen production,[35,36] hydrogen production,[37] CO_2 conversion[38,39] and degradation of pollutants.[40]

Metal-organic frameworks can act as efficient charge carrier transportation systems through a photoexcitation process in organic linkers or metal clusters.[41] Moreover, the optical properties of pure MOFs can easily be tuned by functionalizing the organic linkers (ligands) with other groups such as amino groups which can greatly enhance the visible light harvesting and hence, increase the photocatalytic performance. As shown in Fig. 1, these 3D hybrid materials are constructed from metal nodes (ions or clusters) and organic linkers using different synthesis methods including solvothermal, microwave-assisted, sonochemical, mechanochemical and electrochemical synthesis.

The building blocks of MOFs are formed by linking metal clusters to organic ligands so that an open 3D framework structure is obtained. This geometrically well-defined framework structure endows the materials higher porosity and hence, with an extremely high specific surface area compared to other semiconductors. For instance, in our recent study[42] we found that the titanium-based MOF, NH_2-MIL-125(Ti), exhibited more than 81 times higher specific surface area and 17 times higher pore volume than g-C_3N_4, which is considered as a benchmark photocatalyst in various energy and environmental applications.[43] Moreover, organic linkers in MOFs can provide more visible light absorption and more feasibility for functionalization with other groups, *e.g.* amino group. In terms of synthesis, MOF materials can be grouped into different series including Materials Institute Lavoisier (MILs), Universiteteti Oslo
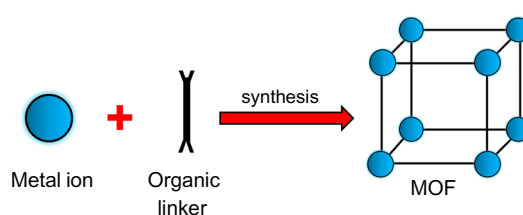
Figure 1. The metal-organic framework structure constructed by metal ions/clusters linked by the organic linkers. Reproduced from Ref. 47 with permission from Elsevier.
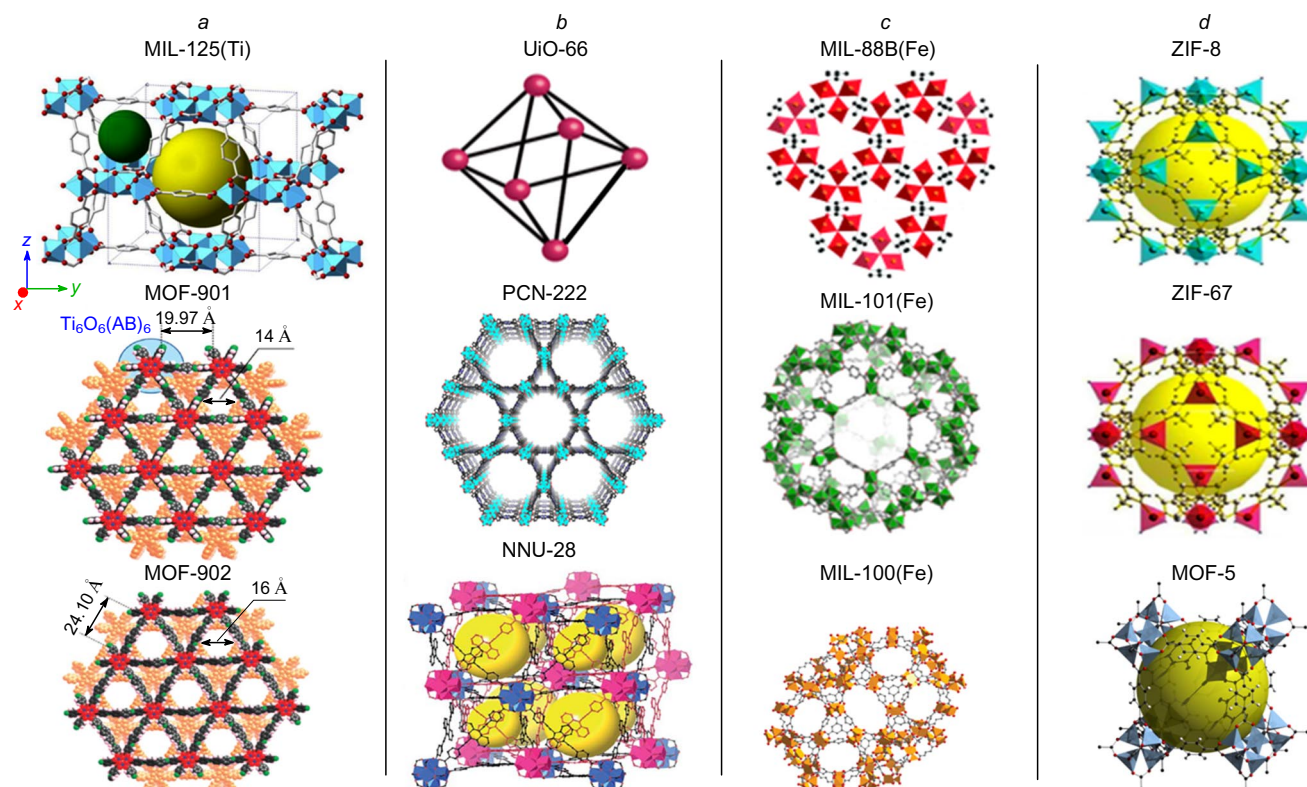
Figure 2. Structures of selected Ti-based MOFs (*a*), Zr-based MOFs (*b*), Fe-based MOFs (*c*) and Zn-based MOFs (*d*). Reproduced from Ref. 47 with permission from Elsevier.
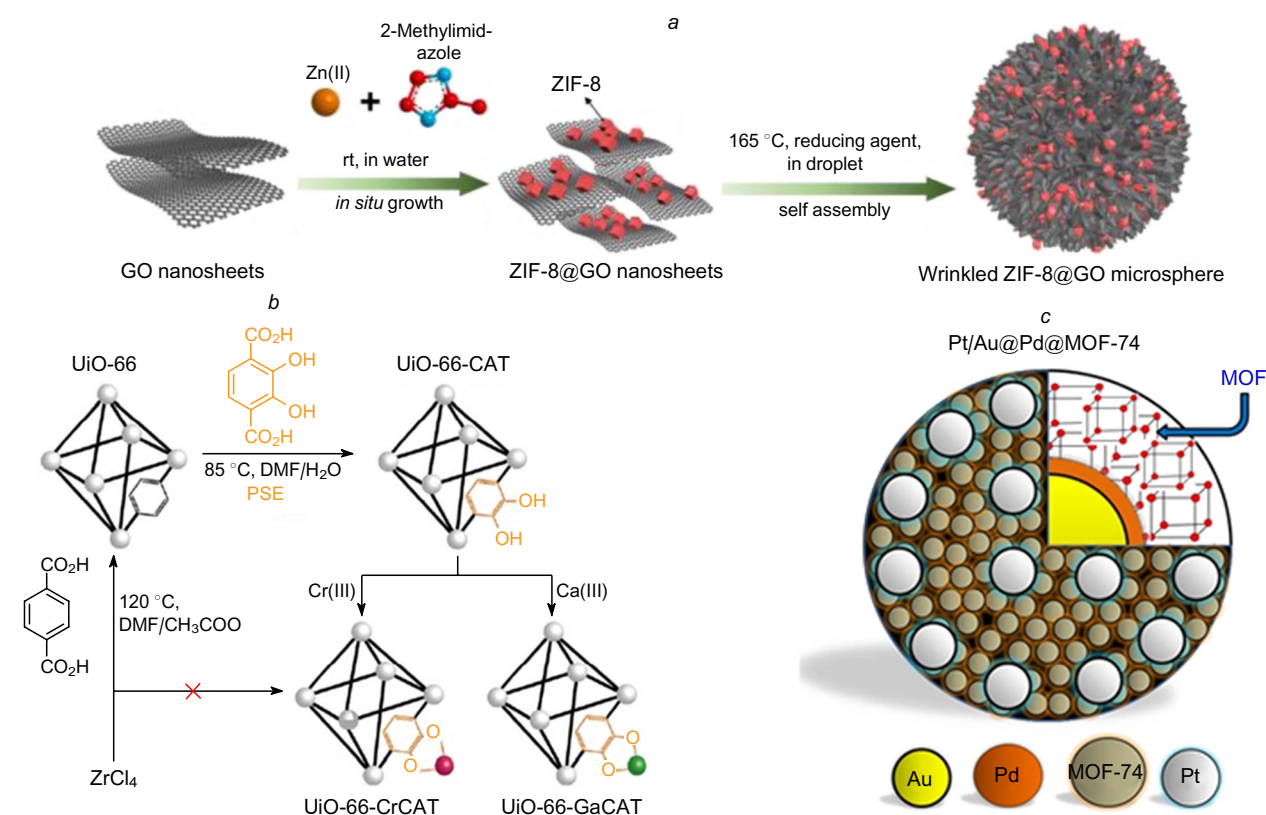
Figure 3. Structural illustration of reduced graphene oxide (GO) nanoparticles doped on ZIF-8 MOF (*a*). Reproduced from Ref. 45 with permission from Wiley. The addition of Cr and Ga metal-monocatecholato (CAT) groups to the linkers of UiO-66 MOF (*b*). Reproduced from Ref. 46 with permission from the Royal Society of Chemistry. PSE is post-synthetic exchange. A metal-MOF composite consisting of Au, Pd, Pt and MOF-74 (*c*). Reproduced from Ref. 47 with permission from Elsevier.

(UiO), Porous Coordination Network (PCN), Northeast Normal University (NNU) and Zeolitic Imidazolate Frameworks (ZIFs).[44]

However, clusters of various metals (mainly transition) such as Ti, Zr, Fe and Zn in the parent MOFs, as shown in Fig. 2 can also be modified by introducing of extra active sites *via* some strategies of doping,[45] metal addition[46] and MOF-based composites[47] (Fig. 3).

These structural and tunable features provide MOFs with unique properties related to a high specific surface area and porosity which rank these materials among all other solids. As porous materials with a high surface area, MOFs are considered as the most ideal adsorbents for the storage and separation of gases (mainly CO_2 and H_2) due to their high physical adsorption capacity. However, the pore size and shape can be predicted, tuned and controlled by analogy with other related MOF structures relative to the ligands size.[48]

Among the studied MOFs, the Fe-based MOFs attracted much attention due to their semiconducting properties, low cost, visible light response, environmental safety, reliable chemical and thermal stability.[49, 50] Generally, the Fe-based MOFs consist of an oxocluster made up of the earth-abundant Fe element obtained from its salts and connected with organic linkers. A wide variety of Fe-based MOFs with different compositions and structures are available, making it easy to study the influence of the composition and structure on the Fe-based MOF photocatalytic activity. Previous limited results have revealed that the photocatalytic performance is affected not only by the nature of the Fe cluster but also the organic linker and the framework topology. For instance, both MIL-100(Fe) and MIL-88B(Fe) MOFs are constructed of similar $Fe_3\mu_3$-oxo clusters and various organic linkers. Although these MOFs exhibited good light absorption in the visible range, MIL-88B(Fe) displayed higher catalytic activity for rhodamine photodegradation compared to MIL-100(Fe).[51]

2.2. Fe-MOF based materials

Generally, the Fe-MOFs based materials as photocatalysts can be divided into three types: Fe-based MOFs, Fe-MOF derivatives and their hybrid nanocomposites (NC). A synergistic effect between Fe and other metals such as Ni, Co, W and Mo can be obtained by the incorporation of Fe-based MOFs and other guest metal atoms, thus providing more metal active sites and hence, better photocatalytic performance.[52] Fig. 4*a* shows the fabrication strategy of Fe-MIL MOF nanorods through a hydrothermal reaction followed by Ni-doping, which then exhibited an enhanced performance for photocatalytic oxygen production.[53]

Fe-based MOFs can also be used as precursors or templates in the thermal-assisted synthesis of functionalized materials with different structures and tailored compositions, including carbon-derived materials such as carbides or, *e.g*., phosphides in addition to hydroxides and metal oxides.[54] As shown in Fig. 4*b*, nanoparticles (NP) of
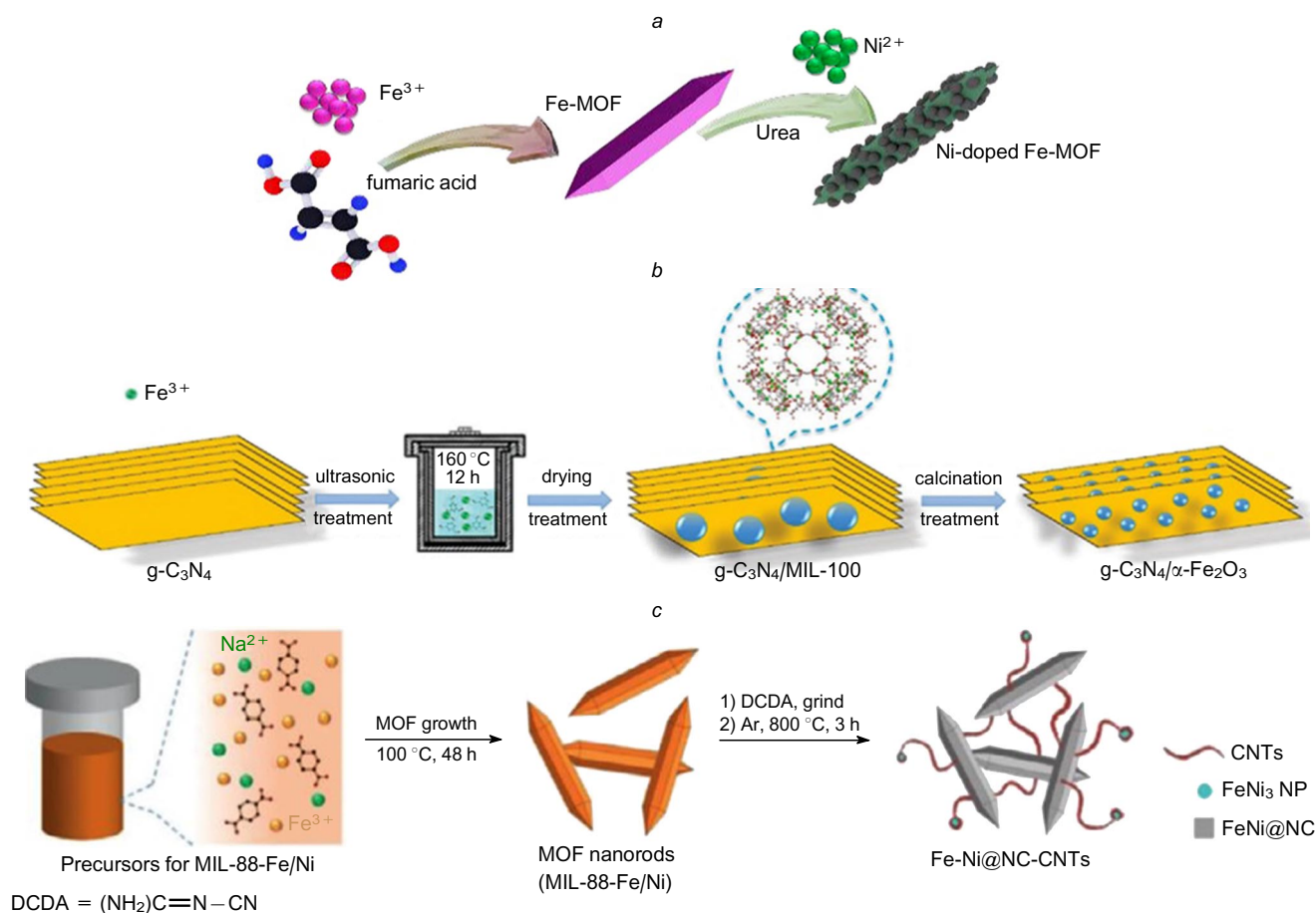
Figure 4. Scheme representation of Fe-MOF preparation followed by Ni-doping (*a*),[53] the synthetic strategy to prepare the Fe-MOF-derived g-C_3N_4/α-Fe_2O_3 nanocomposite (*b*). Reproduced from Ref. 55 with permission from Wiley. Schematic representation of the synthesis of Fe-Ni@NC-CNTs (*c*). Reproduced from Ref. 56 with permission from Wiley.
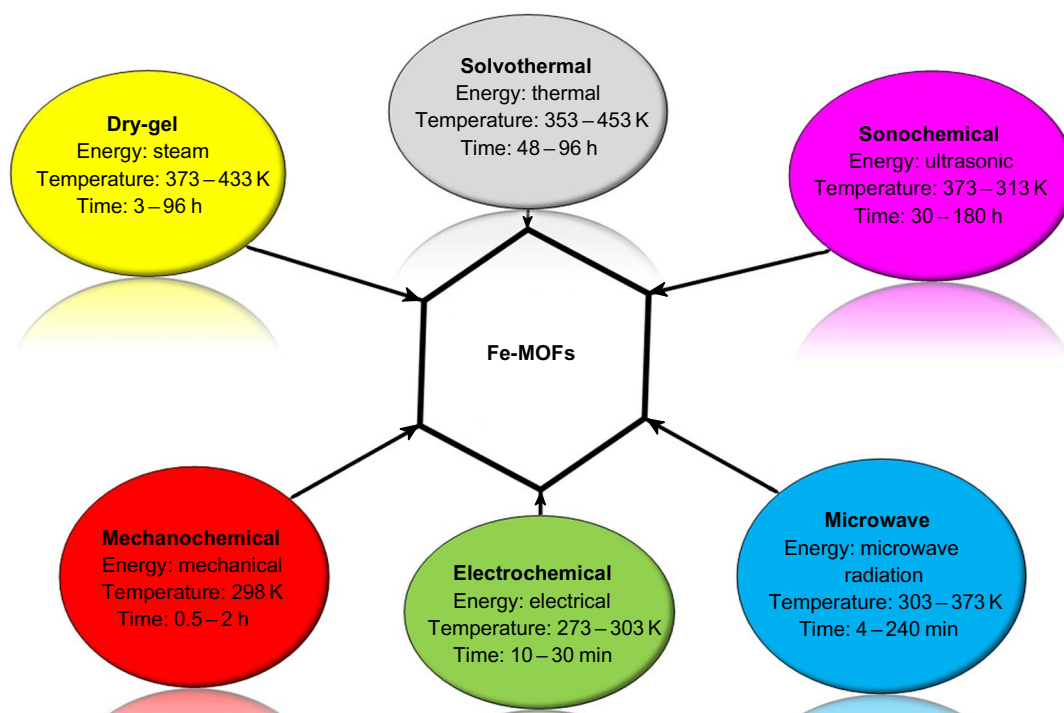
Figure 5. Schematic representation of the main synthesis methods of Fe-based MOFs.

α-Fe_2O_3-coupled g-C_3N_4 were synthesized from a well-known metal-organic framework (MIL-100(Fe)) using an ultrasonication treatment.[55]

Finally, hybridizing Fe-based MOFs with graphene or other functional materials, such as amino or hydroxide groups, is another option to overcome the issues related to Fe-based MOF photocatalysts. In 2018, Thomas and co-authors[56] reported the formation of an efficient Fe-Ni@NC-CNT (CNT is nanotube) hybrid photocatalyst *via* the pyrolysis of dicyandiamide-functionalized MIL-88(Fe)/Ni MOF (Fig. 4c).

2.3. Synthesis of Fe-based MOFs

The choice for a synthetic approach is of great importance in the construction of MOFs since it determines the structure and affects the performance of the resulting MOFs. However, Fe-based MOFs can be synthesized through either conventional or non-conventional routes, where the latter can be carried out *via* six main procedures using various forms of energies and different conditions as illustrated in Fig. 5 and discussed in next sections.

2.3.1. Solvothermal synthesis

This method is the most widespread technique used for the preparation of MOFs. In this approach, the reactants (organic linker, metal salt and solvent) are mixed in certain ratios and heated at temperatures (353–453 K) above the boiling point of the used solvent.[57] This can be carried out in an autoclave, which can provide required reaction conditions for this process, namely, both high temperature and high pressure, where both liquid and gas phases exist simultaneously and thus, converting the reactants into supercritical fluids for boosting the mixing of compounds and promoting the crystal growth.[58] The most commonly used reaction media are organic solvents such as dimethylformamide, diethylformamide (DEF), acetone, methanol and ethanol. However, a mixture of two or more solvents can be used to overcome the problem of insolubility.[59]

Fig. 6a demonstrates the solvothermal synthesis process. Whitefield *et al.*[60] reported a successful synthesis of an Fe-based MOF by a solvothermal method using DMF as the solvent. The crystalline MIL-53(Fe) MOF was obtained after 48 h at 180 °C. Also, Feng *et al.*[61] employed this approach to prepare the PCN-332(Fe) MOF. A certain amount of FeM (15 mg) was ultrasonically dissolved in a mixture of acetic acid (1 mL) and DMF (2 mL), the mixture was then heated in an oven (12 h, 140 °C). After cooling down to room temperature, dark brown crystals were obtained through filtration. This method yielded an extremely stable and highly crystalline Fe-based MOF. Table 1 summarizes the recent advances in the field of Fe-based MOFs prepared by solvothermal and other non-conventional methods.

2.3.2. Sonochemical synthesis

This ultrasound-assisted synthesis method is based on sonochemistry and is used when chemical reactions need to be carried out quickly under ambient conditions. The sonochemical treatment is conducted by subjecting a substrate solution to very high ultrasonic frequencies (20 kHz–10 MHz) to create localized hot spots with extremely high temperature (5000 K) and pressure (1000 bar), which facilitates the chemical process.[83, 84] Compared to the conventional solvothermal approach, this method can provide highly crystalline Fe-MOF materials with a smaller particle size in a short period of time.[85] Fig. 6b illustrates the procedure for the Fe-based MOF synthesis by sonochemical treatment.

An Fe-MOF known as MIL-88A (Fe) was synthesized through a sonochemical approach by Chalati *et al.*[66] with various reaction parameters being analyzed. A comparative study of the MIL-88A MOF synthesis *via* solvothermal, hydrothermal and microwave techniques was also conducted. However, the best results were achieved using the ultrasonic approach, which provided the rapid synthesis with a smaller particle size but in lower yields.
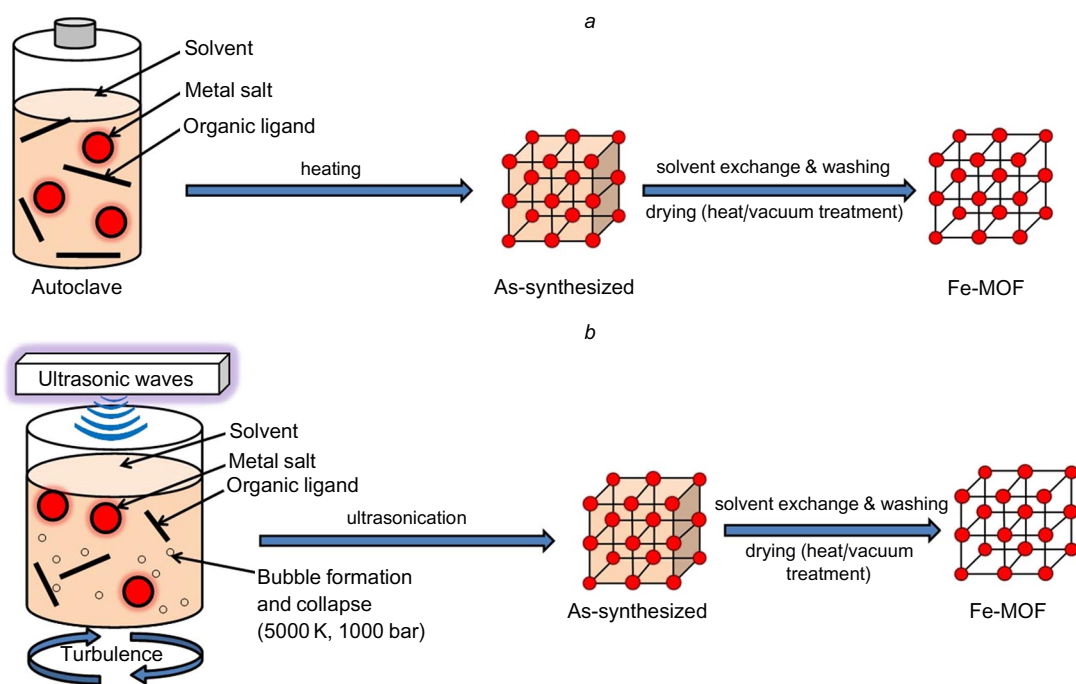
Figure 6. The Fe-based MOF synthesis through the solvothermal method (*a*), the Fe-based MOF synthesis through the sonochemical method (*b*). Reproduced from Ref. 47 with permission from Elsevier.

Table 1. Recent developments of Fe-based MOFs synthesized by different methods under various conditions.

MOF	Preparation method	Solvent	Ligand	Conditions	Ref.
MIL-53(Fe)	Solvothermal	DMF	1,4-Benzenedicarboxylic acid	180 °C, 48 h	60
PCN-250(Fe)	Solvothermal	DMF	Acetic acid	140 °C, 12 h	61
EY-MIL-101(Fe)	Solvothermal	DMF	1,4-Benzenedicarboxylic acid	180 °C, 12 h	62
NH_2-MIL-53(Fe/Co$_{0.75}$)	Solvothermal	DMA	2-Aminoterephthalic acid	150 °C, 3 h	63
PCN-221(Fe$_x$)	Solvothermal	DEF	Tetra(4-carboxyphenyl)porphyrine acid	120 °C, 12 h	64
MIL-101(Fe)	Solvothermal	DMF	1,4-Benzenedicarboxylic acid	110 °C, 24 h	65
MIL-53(Fe)	Solvothermal	DMF	1,4-Benzenedicarboxylic acid	170 °C, 24 h	65
MIL-88(Fe)	Solvothermal	DMF	1,4-Benzenedicarboxylic acid	100 °C, 12 h	65
MIL-88A(Fe)	Sonochemical	Solvent-free	Fumaric acid	0–50 °C, 0.5–2 h	66
PCN-6	Sonochemical	DMF	4,4,4-s-Triazine-2,4,6-triyl-tribenzoic acid	500 W, 20 kHz, 1 h	67
MIL-101(Fe)	Microwave	DMF	1,4-Benzenedicarboxylic acid	150 °C, 10 min	68
NH_2-MIL-101(Fe)	Microwave	DMF	NH_2-1,4-Benzenedicarboxylic acid	150 °C, 15 min	68
MIL-53(Fe)	Microwave	DMF	1,4-Benzenedicarboxylic acid	150 °C, 60 min	69
MIL-101(Fe)	Microwave	DMF	1,4-Benzenedicarboxylic acid	110 °C, 45 min	70
NH_2-MIL-101(Fe)	Microwave	DMF	2-Aminoterephthalic acid	110 °C, 45 min	70
MIL-53(Fe)	Microwave	DMF	—	300 W, 150 °C, 10 min	71
Cr-MIL-100	Microwave	HF	1,4-Benzenedicarboxylic acid	600 W, 210 °C, 60 min	72
MIL-100(Fe)	Electrochemical	H_2O/MeOH	1,3,5-Benzenetricarboxylic acid	110–190 °C, 0–20 mA cm^{-2}	73
Ni/Fe-BTC-MOF	Electrochemical	EtOH	1,3,5-Benzenetricarboxylic acid	25 °C, 10 min, 6.5 pH	74
Fe-BTC	Electrochemical	MeOH	1,3,5-Tricarboxylic acid	32 °C, 55 min, 3.8 A dm^{-2}	75
MIL100(Fe)	Mechanochemical	TMAOH	1,3,5-Benzenetricarboxylic acid	1 h	76
MIL-88A(Fe)	Mechanochemical	Solvent-free	Disodium fumarate	10 min	77
Fe–Pd@C	Mechanochemical	TMAOH	NH_2-1,4-Benzenedicarboxylic acid	1 h	78
MIL-100(Fe)	Mechanochemical	Solvent-free	1,3,5-Benzenetricarboxylic acid	10 min	79
MIL-100(Fe)	Dry-gel	H_2O	1,3,5-Benzenetricarboxylic acid	165 °C, 96 h	80
MIL-100(Fe)	MW-assisted dry-gel	H_2O	1,3,5-Benzenetricarboxylic acid	150 °C, 3 h, 800 W	81
MIL-100(Fe)	Dry-gel	Solvent-free	1,3,5-Benzenetricarboxylic acid	433 K, 24 h	82

Note. EY is eosin Y.

It is also worth mentioning that there are some factors that can greatly affect the properties of the resulting MOF material, such as the applied power, the power supply mode and the ultrasonic generator type. The sonication time has also a significant impact on the crystal growth and nucleation rate, since highly crystalline MOF nanoparticles are formed at short sonication times, while amorphous MOF structures are obtained at longer times.[86, 67]

2.3.3. Microwave synthesis

The microwave-assisted synthesis is considered as an important method that can be employed for the rapid synthesis of Fe-based MOFs.[87] In the microwave-assisted mode, the

R.R.Ikreedeegh
Russ. Chem. Rev., 2022, **91** (12) RCR5064

7 of 20
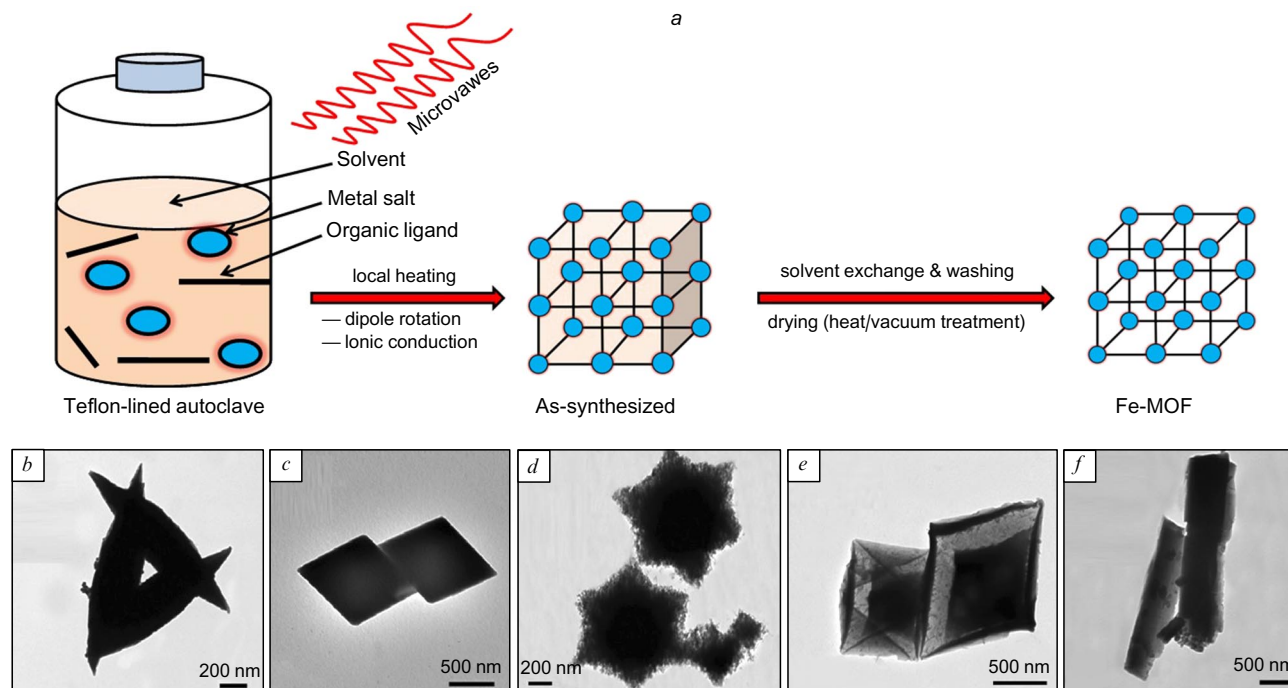
Figure 7. Scheme of the synthesis of Fe-based MOFs through a microwave method (*a*); TEM images of MIL-53(Fe)-0.5h (*b*), MIL-53(Fe)-1h (*c*), MIL-53(Fe)-3h (*d*), MIL-53(Fe)-6h (*e*) and MIL-53(Fe)-12h (*f*). Reproduced from Ref. 69 with permission from the American Chemical Society.

solution is heated at a temperature ranging from 303 to 373 K under high-frequency microwave irradiation.[88] A uniform rise in the reaction temperature results in MOF crystallization within a few minutes with controlled crystal shape and size. Compared to the solvothermal synthesis, this method provides much faster preparation of high-quality MOFs. For example, the MIL-53(Fe) MOFs can be synthesized by microwave heating in as little as 5 to 10 min, while the solvothermal method takes 15 h.[89] The microwave-assisted process is illustrated in Fig. 7 *a*. A very significant study on the synthesis and functionalization of the MIL-101(Fe) MOF using the microwave procedure was reported by Taylor-Pashow *et al.*[68] The obtained product displayed an unusual octahedron morphology and crystal-line nanostructure with a high specific surface area reaching up to 4535 m^2 g^{-1}. Using a microwave-assisted hydrother-mal technique, Guo *et al.*[69] investigated the effect of the reaction time on the morphology and properties of the resultant MIL-53(Fe) MOF samples. It was found that the porosity and morphology of the products vary with the microwave irradiation time (0.5, 1, 3, 6 and 12 h). As shown in Fig. 7 *b*–*f*, various morphologies of spindle, uniform spindle, solid octahedron, yolk–shell octahedron and nano-rods were obtained by changing the irradiation time.

2.3.4. Electrochemical synthesis

The electrochemical synthesis method is based on the conversion of electrical energy to chemical energy through an electrochemical set-up shown in Fig. 8 *a* under mild operating conditions of temperature, pressure and pH. Controlling the applied voltage and current also helps to carry out a controlled reaction in a short period of time making this method one of the industrial scale-up methods for the production of Fe-based MOFs. Generally, the electrochemical method involves two main variants,

namely, the anodic dissolution method and the cathodic deposition. In the anodic dissolution, the desired metal is employed as an anode while the organic linker is dissolved in the solvent (reaction medium).[75] In contrast, in the cathodic approach both the organic linker and the metal ion are dissolved in the reaction medium, which then interacts with a cathode.[90]

Campagnol *et al.*[73] used an electrochemical approach to prepare the MIL-100(Fe) MOF. The study of the influence of the temperature change (110–190 °C) on the crystals shape and size revealed that lower temperatures (110–130 °C) led to the formation of polydisperse crystals ranging in size from 50 nm to 1 μm, while only small monodisperse crystals were obtained at higher temperatures (170–190 °C) as shown in Fig. 8 *b*–*d*. Also, some other parameters such as the applied current, the deposition time and the presence of tributylmethylammonium methyl sul-fate (MTBS) as a conductive compound were investigated. In 2020, Pourfarzad *et al.*[74] fabricated a novel bimetallic benzenetricarboxylic (BTC) metal-organic framework named as Ni/Fe-BTC MOF *via* an electrochemical approach. The newly synthesized composite was used as a bifunctional oxygen electrocatalyst, which exhibited excep-tional electrical conductivity and chemical adaptability.

2.3.5. Mechanochemical synthesis

In 2006, Pichon *et al.*[91] pioneered in the mechanochemical synthesis of MOFs. This technique is a solvent-free approach providing high yields and waste-free production, which makes it a potential competitor for industrial scale-up productions compared with other methods. In the mechanochemical synthesis route, the reaction is carried out by applying the mechanical energy, which induces the breakage of the intramolecular bonds of the reactants resulting in a chemical transformation within a short period
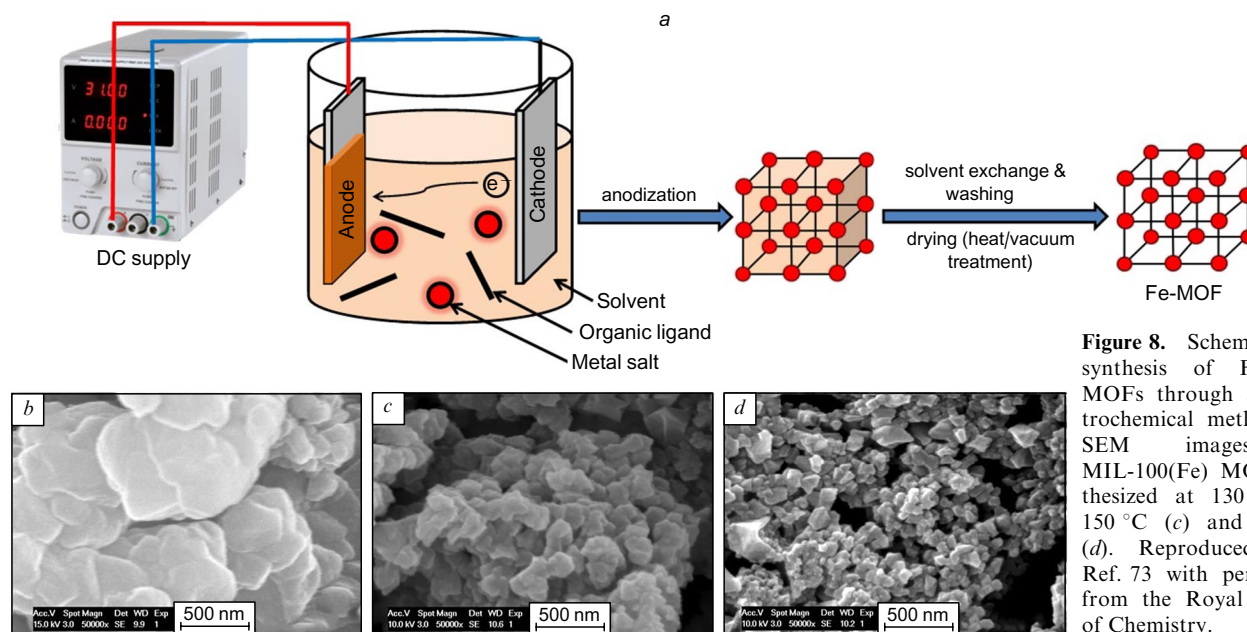
Figure 8. Scheme of the synthesis of Fe-based MOFs through an electrochemical method (*a*); SEM images of MIL-100(Fe) MOF synthesized at 130 °C (*b*), 150 °C (*c*) and 190 °C (*d*). Reproduced from Ref. 73 with permission from the Royal Society of Chemistry.

of time (from 10 min to 1 h).[92] Generally, the mechanochemical approaches can be divided into two groups: (a) neat grinding (NG), in which the process is conducted in the complete absence of solvent and (b) liquid-assisted grinding (LAG), which involves the addition of minor amounts of solvent into the solid reaction mixture.[93] However, it was found that in the LAG process, 1D, 2D and 3D-coordination polymers can be obtained from the same reaction mixture by varying the amount of the solvent.[94–96] Fig. 9 *a* shows the procedure for Fe-based MOF synthesis through a mechanochemical method.

The synthesis of the MIL-100(Fe) MOF through a liquid-assisted grinding method was reported by Pilloni

et al.[76] In this study, an aqueous alkaline solution of tetramethylammonium hydroxide (TMAOH) was used to increase the yield and avoid the presence of unreacted H_3BTC acid in the final product. The mechanochemically synthesized composite displayed a high surface area, enhanced crystallinity and thermal stability.

Recently, a comparative study has been carried out on the synthesis of the MIL-88A(Fe) MOF using various types of solvents (triethylene glycol, H_2O, solution-phase and solvent-free) in the mechanochemical process.[77] It was found that the presence of a medium during the synthesis of Fe-MIL-88A(Fe) has a great impact on the morphology formation and the crystal growth. However, the
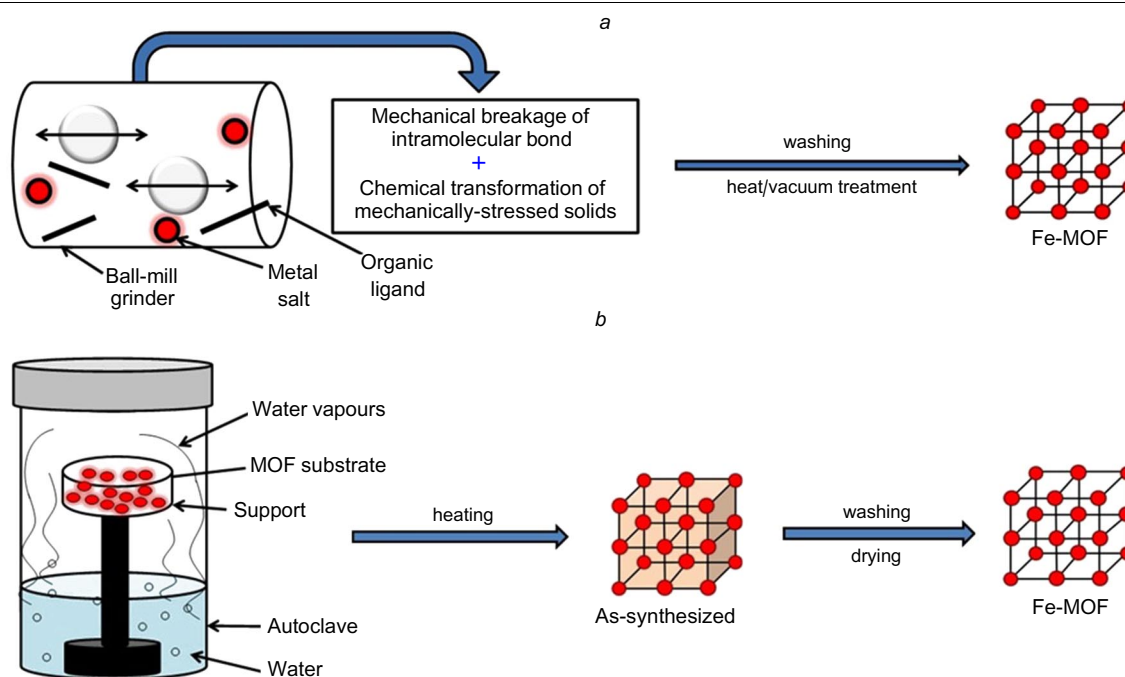
Figure 9. The procedure of Fe-based MOF synthesis through the mechanochemical method (*a*), dry sol–gel method (*b*). Reproduced from Ref. 47 with permission from Elsevier (Fig. 9 *a*).

R.R.Ikreedeegh
Russ. Chem. Rev., 2022, **91** (12) RCR5064

9 of 20

MIL-88A(Fe) MOF prepared *via* a solvent-free mechanochemical procedure displayed a rod-like microparticle structure with the highest surface area (108.42 m^2 g^{-1}) compared to that of the other MIL-88A(Fe) MOF samples prepared under other mechanochemical conditions.

Also, He *et al.*[78] reported the synthesis of a Fe-MOF-derived nanocomposite named as (Fe−Pd@C) using a fast and simple mechanochemical approach. The pyrolysis of the Fe-based MOF precursor afforded an efficient carbonized catalyst with an exceptional catalytic performance, good stability and extended catalyst life time.

2.3.6. Dry-gel synthesis

The idea of dry-gel conversion (DGC), also known as steam-assisted conversion (SAG) was first discovered by the zeolite research group of Xu *et al.*[97] In this technique, the Fe-MOF is formed by the contact of the MOF precursor with water vapours (Fig. 9 *b*).[98] Compared to other conventional MOF synthesis methods, the DGC has some advantages such as minimum waste disposal, higher concentrations of reactants in the reaction medium, the controlled shape and structure of the resulting MOFs and the possibility of continuous production.[99] It is also worth mentioning that the used solvent in DGC can also be reused in multiple synthesis cycles without affecting the yield and quality of the formed MOF crystals.[79]

Ahmed *et al.*[80] used the dry-gel conversion to prepare the MIL-100(Fe) MOF. In this study, a mixed gel of Fe/H$_3$BTC was placed on a porous holder placed inside an autoclave containing water. The autoclave is then heated in an oven at 165 °C so that the dry gel is treated with steam to give a crystalline MOF material with a high surface area and pore volume. It was also observed that the crystallinity of the product increases with increasing the heating time up to a certain value.

Tannert *et al.*[81] also synthesized the MIL-100(Fe) MOF through a novel and facile microwave-assisted DGC technique. Compared to the above-mentioned study,[80] the MOF production was achieved in a shorter reaction time at a lower temperature. Moreover, the obtained MIL-100(Fe) MOF exhibited a Brunauer−Emmett−Teller (BET) surface area reaching up to 1287 m^2 g^{-1}.

In 2020, Luo *et al.*[82] investigated the effect of absence of a solvent (water) on the crystallinity, morphology, pore structure, adsorption and desorption capacity of the dry-gel synthesized MIL-100(Fe) MOF. The prepared Fe-BTC dry gel was placed in a sealed glass jar and heated at 165 °C for 24 h. It was found that the BET specific surface area gradually decreases with the decrease in the reactive sol concentration. However, the maximum specific surface area of 1736 m^2 g^{-1} was obtained with zero a sol concentration.

3. Photocatalytic applications of Fe-based MOFs

3.1. Photocatalytic oxygen production

Among all MOF types, Fe-based MOFs are considered to be extremely attractive materials, since, firstly, iron is an earth-abundant element, secondly, the presence of large iron oxo clusters make almost all Fe-based MOFs visible-light-responsive materials compared to other MOFs such as Ti- and Zr-containing MOFs, this property being attributed to the direct excitation caused by the Fe−O metal clusters.[65] All these advantages make the Fe-containing MOFs, in particular, promising materials in the field of photocatalysis. In Fe-based MOFs, the photocatalytic oxygen evolution reactions (OER) can be represented by the following equations:

$$Fe\text{-}MOF + h\nu \longrightarrow Fe\text{-}MOF(e^-) + Fe\text{-}MOF(h^+) \quad (1)$$

$$2\,H_2O + 4(h^+) \longrightarrow O_2 + 4\,H^+ \quad (2)$$
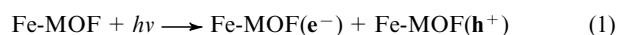
Shah *et al.*[100] reported a successful encapsulation of two different cobalt-functionalized polyoxometalate (POM) anions in the MIL-100(Fe) MOF as shown in Fig. 10 *a*. The POMs anions were referred to as Co2 for [Co^{II}Co^{III}W$_{11}$O$_{39}$(H$_2$O)]$^{7-}$ and Co4 for [Co$_4$(PW$_9$O$_{34}$)$_2$(H$_2$O)$_2$]$^{10-}$. Interestingly, these two POM-MOF composites exhibited greater enhanced photocatalytic water oxidation ability compared to their individual components. This was explained by the integration of the MIL-100(Fe) MOF which addressed the issue of POM solubility. The synergic effect of electrostatic interactions between the guest units (POM) and the host material (Fe-MOF) also played an important role in improving the overall photocatalytic performance. The proposed mechanism for photocatalytic oxygen evolution is illustrated in Fig. 10 *b*. When light is applied to the photocatalyst surface, it undergoes an excitation and generates a population of photogenerated charges; these electrons (e$^-$) are transferred from the LUMO of the MIL-100(Fe) MOF to its HOMO, leaving holes (h$^+$) in LUMO, which then oxidize water to produce oxygen. The POM units provide an additional pathway for the transfer of photogenerated charges by accepting electrons from the MOF HOMO into the conduction band (CB) of POM. The POM units are most likely to exist in close proximity to the MIL-100(Fe) μ$_3$-O bridged Fe$_3$ units due to electrostatic interactions between the anionic POM and the Lewis-acidic Fe$_3$ units, thereby promoting more efficient electron transfer from LUMO of the MIL-100(Fe) MOF to its HOMO and hence improving the photocatalytic water oxidation process.

Qu *et al.*[101] reported the preparation of a Fe-based MOF known as MIL-53(Fe). This photocatalyst exhibited good photocatalytic evolution for oxygen production under visible light irradiation. However, higher O$_2$ evolution of 120 μmol was also obtained by functionalizing the MOF with an amino group (NH$_2$). The NH$_2$-MIL-53(Fe) composite displayed an O$_2$ evolution of 120 μmol after 140 min; this improvement was attributed to the final narrower bandgap and to the more efficient separation of photogenerated electron−hole pairs.

A new MOF-derived nanotube composite (Fe−Ni−P) was synthesized by Li *et al.*[102] using bimetallic Fe-Ni-MIL-88(Fe) nanorods as the template. The resulting nanotubes were integrated with two different dyes based on tris(bipyridine) ruthenium(II) [Ru(bpy)$_3$]$^{2+}$ and S$_2$O$_8^{2-}$ as a both visible light absorber and an electron sacrificial agent, respectively.

The maximum O$_2$ amount (900.3 μmol g^{-1} h^{-1}) was achieved; however, the photocatalytic activity for the O$_2$ production depended on the Fe/Ni ratio in the Fe−Ni−P nanotubes. The same composite, was further tested for the H$_2$ production under similar conditions but using different dyes and sacrificial agents and was demonstrated to exhibit the production of 5420 μmol g^{-1} h^{-1}.

In 2019, Lionet *et al.*[103] synthesized nine different functionalized iron-based MOFs using the MIL-88B(Fe) MOF structure with multiple linkers (−4 H, −Br, −NO$_2$, −NH$_2$, −OH, −4 F, −4 Me, −2 Me, −2 OH) as shown in

Figure 10. The synthesis of two POMs encapsulated in the MIL-100(Fe) MOF (*a*), the proposed reaction mechanism for photocatalytic oxygen production under visible light irradiation (*b*). Reproduced from Ref. 100 with permission from Elsevier. Types of linkers employed to prepare the MIL-88B(Fe) MOFs (*c*), Amount of O_2 produced by the different iron-based MOFs after 2 h of visible light irradiation (*d*). Reproduced from Ref. 103 with permission from the American Chemical Society.

Fig. 10 *c*. Clearly, the tetrafluoroterephthalic-based MOF exhibited the highest photocatalytic O_2 production (30 µmol) which is 5 times higher than that of the pristine MIL-88B(Fe) MOF as depicted in Fig. 10 *d*. This enhancement in the photocatalytic activity was found to be attributed to the hydroxylation rate of the organic linkers that can be altered by introducing activating or deactivating groups into the benzene ring.

A series of Fe-based MOFs with three different topological structures bearing the same functional ligands, specifically, MIL-53(Fe), MIL-88B(Fe) and MIL-101(Fe), were investigated for visible-light-driven photocatalytic oxygen evolution with the use of $[Ru(bpy)_3]^{2+}$ as a photosensitizer and $Na_2S_2O_8$ as an electron acceptor.[104] Also, the performance of these three pristine photocatalysts was compared to that of their amino-functionalized derivatives. However, the highest O_2 evolution of 36.5 µmol was achieved using the MIL-101(Fe) MOF. The effect of water pH on the photocatalytic oxygen evolution was also studied

and found to increase with the pH increase (up to pH 10), since higher pH values are thermodynamically favourable for water oxidation reactions. However, at pH 11, a significant decrease in O_2 evolution was observed, which may be due to the degradation of the $[Ru(bpy)_3]^{2+}$ photosensitizer at higher pH values.

Various Fe-based MOF photocatalysts such as MIL-101(Fe), MIL-53(Fe), MIL-88(Fe), MIL-100(Fe) and MIL-126(Fe) were also tested for photocatalytic water oxidation by Horiuchi *et al.*[105] Among all tested samples, the MIL-101(Fe) MOF displayed the highest O_2 evolution (14.7 µmol, 9 h visible light irradiation) with the use of $AgNO_3$ as a sacrificial agent. The photocatalytic reactivity can be attributed to the limited recombination rate of charge carriers resulting from the formation of finely dispersed Fe-oxo clusters embedded as nodes of the porous framework and also due to the largest pore diameter exhibited by the MIL-101(Fe) MOF. The photocatalytic O_2 production performances of the typical Fe-based MOFs

R.R.Ikreedeegh
Russ. Chem. Rev., 2022, **91** (12) RCR5064

11 of 20

Table 2. Recent developments of Fe-MOFs and Fe-MOF composites for photocatalytic O_2 production.

Photocatalyst(s)	Feed composition	Light source Power Wavelength Intensity	Reactor Parameters	Production rate	Ref.
NH_2-MIL-53(Fe)	0.70 mM catalyst 1.0 mM [Ru(bpy)$_3$]Cl$_2$ 0.08 M Na$_2$S$_2$O$_8$ 20 mM buffered H$_2$O	Visible light 4 W LED lamp $450-550$ nm	Glass photolysis vessel Time = 140 min pH 8.5	51.44 μmol h^{-1}	101
Fe$-$Ni$-$P nanotubes	5 mg catalyst 20 mg [Ru(bpy)$_3$]Cl$_2\cdot$6 H$_2$O 79.4 mg Na$_2$S$_2$O$_8$ 5 mL Na$_2$HPO$_4$	Visible light 300 W Xe lamp 420 nm 100 mW cm^{-2}	Pyrex reaction cell Vol. = 30 mL pH 7.1	900.3 μmol g^{-1} h^{-1}	102
MIL-88$-$4F	20 mg catalyst 3 mL 0.1 M AgNO$_3$ sol.	Visible light 500 W Xe lamp 420 nm 600 mW cm^{-2}	Self-made Pyrex cell Time = 2 h	750 μmol g^{-1} h^{-1}	103
MIL-88-NO$_2$	20 mg catalyst 3 mL 0.1 M AgNO$_3$ sol.	Visible light 500 W Xe lamp 420 nm 600 mW cm^{-2}	Self-made Pyrex cell Time = 2 h	225 μmol g^{-1} h^{-1}	103
MIL-88-Br	20 mg catalyst 3 mL 0.1 M AgNO$_3$ sol.	Visible light 500 W Xe lamp 420 nm 600 mW cm^{-2}	Self-made Pyrex cell Time = 2 h	175 μmol g^{-1} h^{-1}	103
MIL-101(Fe)	1 mg catalyst 10 mL reaction solution (H$_2$O + [Ru(bpy)$_3$]$^{2+}$ + Na$_2$S$_2$O$_8$)	Visible light 300 W Xe lamp 420 nm	Reaction flask Vol. = 20 mL T = 20 °C pH 10 Time = 10 min	219 009 μmol g^{-1} h^{-1}	104
MIL-101(Fe)	10 mg catalyst 3 mL 0.1 M AgNO$_3$ aq. sol.	Visible light 500 W Xe lamp 420 nm 122 mW cm^{-2}	Pyrex glass cell Time = 9 h	163.33 μmol g^{-1} h^{-1}	105

and composite photocatalysts based thereon are summarized in Table 2.

3.2 Photocatalytic hydrogen production

The environmental pollution, fossil fuels depletion and growing energy demand have turned hydrogen generated by photocatalytic water splitting into one of the cheapest and cleanest alternatives to energy productions. Huge efforts have been directed towards the synthesis of heterogeneous photocatalysts for photocatalytic H$_2$ evolution with high efficiency and stability. However, it was established that the photocatalytic H$_2$ production depends entirely on visible light harvesting, energy bandgap positions, charge recombination rate and the availability of active sites.[106] In 2009, MOFs were first applied in the photocatalytic production of hydrogen from water under visible light irradiation. [107] Subsequently, García and co-authors [108] reported two Zr-based MOFs (UiO-66 and NH$_2$-UiO-66) for the photocatalytic production of hydrogen in methanol or water/methanol mixture under visible light irradiation. Since then, the use of MOFs as photocatalysts, including Fe-based MOFs, for the photolysis of water to produce hydrogen has become a research hotspot.

Iron-based MOFs consist mainly of iron-oxo clusters, which act as efficient active moieties for photocatalytic water splitting due to the uniform and highly dispersed small clusters. These clusters shorten the migration pathways between the photogenerated charge carriers and reactant molecules thereby improving the photocatalytic performance. Moreover, the porous structure of Fe-based MOFs greatly contributes to the improved diffusion of reactants.[105]

However, Fe-based MOF photocatalysts have insufficiently negative conduction band positions compared to the redox potential of water reduction,[109] which is considered to be one of the main obstacles to their application. Nevertheless, to solve this issue, a dye-sensitization strategy can be implemented, leading to a more efficient H$_2$ production, in which energetic electrons can be effectively injected into Fe-MOFs *via* dye sensitization thereby lifting up the MOF quasi-Fermi level to overcome the kinetic barrier. This was recently proved by Li *et al.*[62] through sensitizing three different Fe-based MOFs (MIL-101(Fe), MIL-88B(Fe) and MIL-53(Fe)) with Eosin Y dye for the efficient photocatalytic H$_2$ production.

Dai *et al.*[63] synthesized a novel hybrid Fe-based MOF nanocomposite named ZnIn$_2$S$_4$@NH$_2$-MIL-53(Fe/Co$_{0.75}$) with high photocatalytic performance of water splitting for hydrogen production under visible light irradiation (26954.13 μmol g^{-1} h^{-1}). Different amounts of 1.875, 3.75, 7.5 and 15 mg of the Co-doped amino-functionalized MIL-53(Fe) MOF were coupled with ZnIn$_2$S$_4$ (referred to as 0.25, 0.5, 1 and 2 respectively, in Fig. 11 *a*) to improve the visible light response. This efficiently promoted the transfer

12 of 20

R.R.Ikreedeegh
Russ. Chem. Rev., 2022, **91** (12) RCR5064
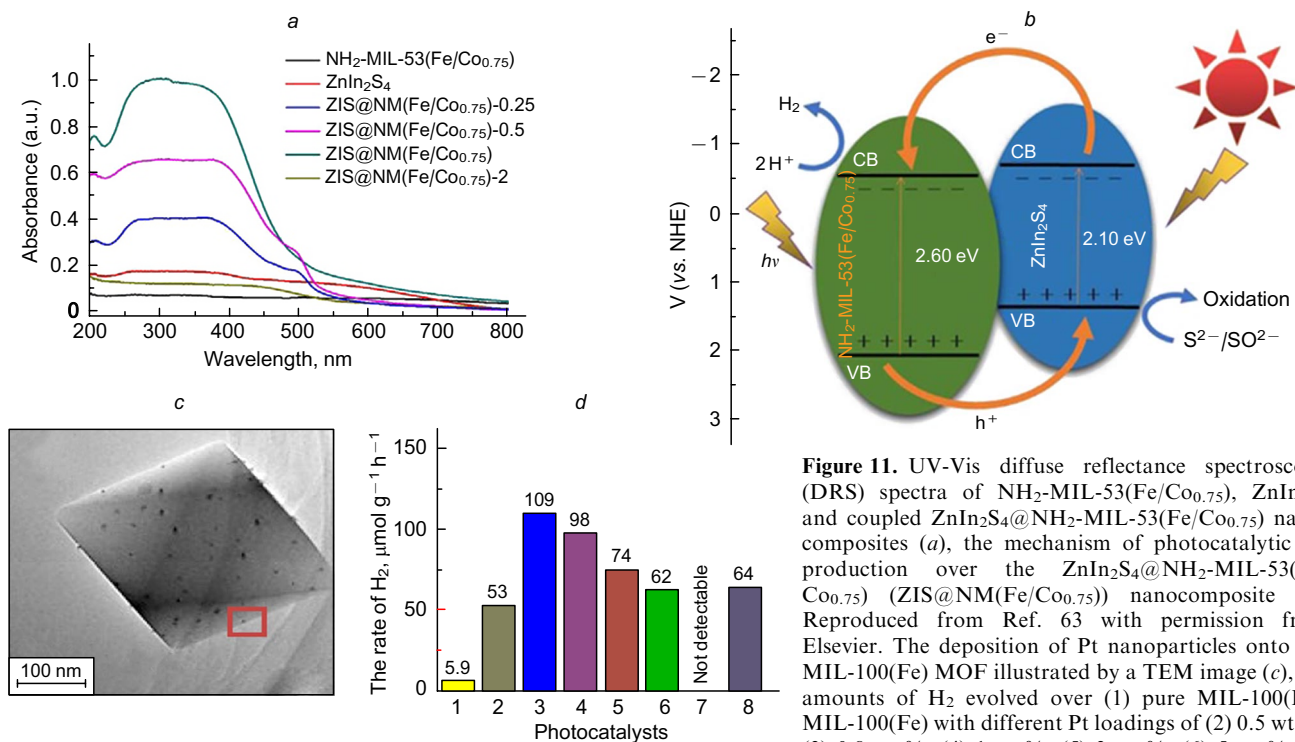
Figure 11. UV-Vis diffuse reflectance spectroscopy (DRS) spectra of NH_2-MIL-53(Fe/$Co_{0.75}$), $ZnIn_2S_4$ and coupled $ZnIn_2S_4$@NH_2-MIL-53(Fe/$Co_{0.75}$) nanocomposites (*a*), the mechanism of photocatalytic H_2 production over the $ZnIn_2S_4$@NH_2-MIL-53(Fe/$Co_{0.75}$) (ZIS@NM(Fe/$Co_{0.75}$)) nanocomposite (*b*). Reproduced from Ref. 63 with permission from Elsevier. The deposition of Pt nanoparticles onto the MIL-100(Fe) MOF illustrated by a TEM image (*c*), the amounts of H_2 evolved over (1) pure MIL-100(Fe); MIL-100(Fe) with different Pt loadings of (2) 0.5 wt.%, (3) 0.8 wt.%, (4) 1 wt.%, (5) 3 wt.%, (6) 5 wt.%, (7) pure Pt nanoparticles and (8) 1 wt.% Pt/MIL-100(Fe)-$NaBH_4$ (*d*). Reproduced from Ref. 110 with permission from the Royal Society of Chemistry.

and separation of photogenerated charges and thus increased the hydrogen production rate. As shown in Fig. 11 *b*, a typical n-type heterojunction photocatalyst was formed with a more negative valence band (VB) and CB of $ZnIn_2S_4$, upon light irradiation, the electrons are excited in both NH_2-MIL-53(Fe/$Co_{0.75}$) and $ZnIn_2S_4$. The photogenerated electrons are then transferred from the $ZnIn_2S_4$ CB to the NH_2-MIL-53(Fe/$Co_{0.75}$) CB and reduce H^+ to produce H_2. However, the photogenerated holes on the MOF VB migrate to the VB of $ZnIn_2S_4$.

A photocatalytic hydrogen production of 5.9 mmol g^{-1} h^{-1} was reported for the MIL-100(Fe) Fe-based MOF under visible light irradiation in a methanol–water mixture.[110] However, an enhanced photocatalytic hydrogen evolution (109 mmol g^{-1} h^{-1}) was observed by depositing Pt nanoparticles onto the pure MIL-100(Fe), which acted as a co-catalyst (Fig. 11 *c*). As shown in Fig. 11 *d*, the optimum H_2 evolution was achieved with Pt nanoparticle loading of 0.8 wt.%.

A series of noble metal-free $NiSe_2$ nanosheet-modified MIL-53(Fe) microrods with different $NiSe_2$ amounts were synthesized *via* a two-step solvothermal procedure and tested for the photocatalytic H_2 evolution.[111] The highest H_2 production of 10.31 mmol h^{-1} g^{-1} was achieved with 1.0 wt.% $NiSe_2$ loading under visible light irradiation, which is more than 11 times higher compared to the pristine MIL-53(Fe) MOF. The $NiSe_2$ nanosheets acted as a co-catalyst and greatly boosted the photocatalytic activity of the MIL-53(Fe) MOF by enhancing the transfer and separation efficiency of photogenerated charge carriers in the $NiSe_2$/MIL-53(Fe) composite as it was revealed by the photoluminescence (PL) spectra and photocurrent analysis (Fig. 12 *a* and *b* respectively).

A novel Z-scheme photocatalyst was fabricated hydrothermally with anchored $CdLa_2S_4$ nanoparticles on the microrod surface of the MIL-88A(Fe) MOF as illustrated in Fig. 12 *c*–*e*.[112] The $CdLa_2S_4$/MIL-88A(Fe) nanocomposite displayed remarkable photocatalytic H_2 evolution of 7677.5 μmol h^{-1} g^{-1} under visible light irradiation, which is about 8 times higher compared to pristine $CdLa_2S_4$. The enhanced photocatalytic activity was attributed to the formed Z-scheme heterojunction, which resulted in the efficient separation and transfer of photogenerated electron-hole pairs. In a Z-scheme photocatalyst system, electrons are transferred in a way similar to the Z-scheme, thereby facilitating the migration of electrons. This system consists of one oxidation photocatalyst (PC I) with a low CB position and another reduction photocatalyst (PC II) with a high VB position. During the light-induced excitation process, the electrons in the PC I are generated and transferred from the VB of PC I to its CB and recombined at the heterostructure interface with the holes in the VB of PC II and are again excited and transferred to the PC II CB to reduce the reactant molecules.

Another ternary-shelled, MIL-88A(Fe)-derived nanotube photocatalyst for photocatalytic water splitting was prepared by Zhao *et al.*[113] Nanosheets of $ZnIn_2S_4$ were grown *in situ* on the surface of MOF-derived Ni-Fe LDH. The resulting ZIS@Ni-Fe LDH nanocomposite exhibited a photocatalytic H_2 production of 2035.81 μmol g^{-1} h^{-1} under visible light irradiation. The hierarchical heterostructure provided a larger surface area, more inner space, more active sites, increased light harvesting and better interfacial electron transfer. Table 3 summarizes the recent developments of Fe-based MOFs and their composites for the photocatalytic hydrogen production.

R.R.Ikreedeegh
Russ. Chem. Rev., 2022, **91** (12) RCR5064

13 of 20
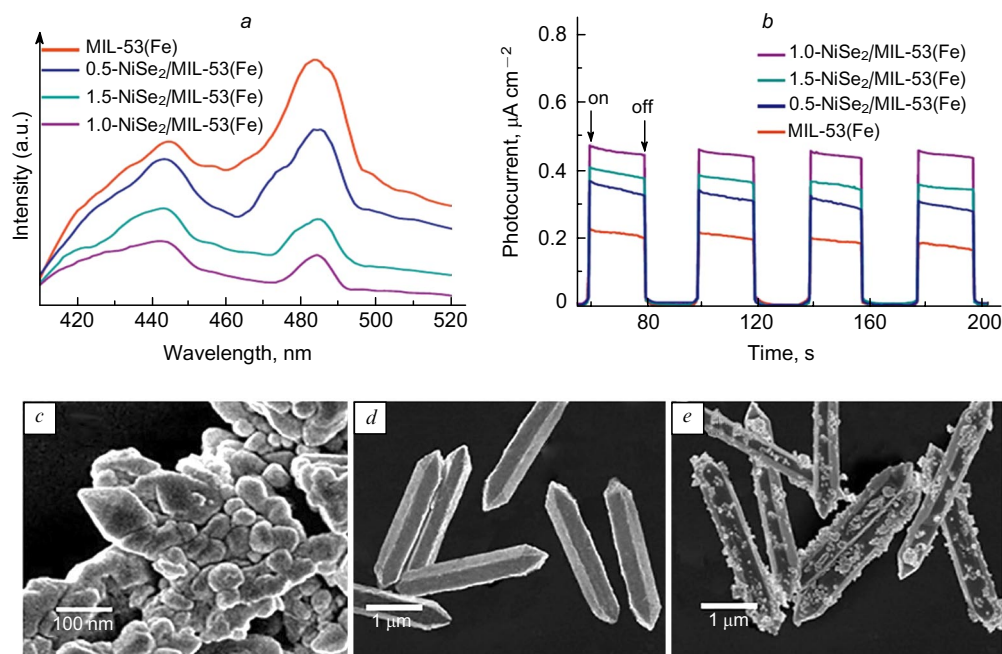
Figure 12. PL spectra (*a*), transient photocurrents (*b*) of pure MIL-53(Fe) and NiSe$_2$/MIL-53(Fe) samples. Reproduced from Ref. 111 with permission from Elsevier. SEM images of CdLa$_2$S$_4$ (*c*), MIL-88A(Fe) (*d*) and CdLa$_2$S$_4$/MIL-88A(Fe) (*e*). Reproduced from Ref. 112 with permission from Elsevier.

Table 3. Recent developments of Fe-MOFs and Fe-MOF composites for photocatalytic H$_2$ production.

Photocatalyst(s)	Feed composition	Light source Power Wavelength Intensity	Reactor Parameters	Production rate	Ref.
Fe−Ni−P nanotubes	5 mg catalyst 20 mg EY 1 mL triethanolamine (TEOA) 9 mL H$_2$O	Visible light 300 W Xe lamp 420 nm 100 mW cm^{-2}	Pyrex reaction cell Vol. = 30 mL	5420 µmol g^{-1} h^{-1}	102
EY-MIL-101(Fe)	5 mg catalyst 20 mg EY 1 mL TEOA 9 mL H$_2$O	Visible light 300 W Xe lamp 400−550 nm 100 mW cm^{-2}	Pyrex flask Vol. = 30 mL pH 7 Time = 2 h	315 µmol g^{-1} h^{-1}	62
MIL-101(Fe)	5 mg catalyst 20 mg EY 1 mL TEOA 9 mL H$_2$O	Visible light 300 W Xe lamp 400−550 nm 100 mW cm^{-2}	Pyrex flask Vol. = 30 mL pH 7 Time = 2 h	9.95 µmol g^{-1} h^{-1}	62
ZnIn$_2$S$_4$@ NH$_2$-MIL-53(Fe/Co$_{0.75}$)	20 mg catalyst 3 mL 0.1 M AgNO$_3$ sol. 100 mL deionized water (0.35 M Na$_2$S and 0.25 M Na$_2$SO$_3$) 0.5 wt.% Pt cocatalyst	Visible light 500 W Xe lamp 420 nm	Quartz flask Vol. = 150 mL	26954.13 µmol g^{-1} h^{-1}	63
Pt/MIL-100(Fe)	45 mg catalyst 22.5 mL water/MeOH (v/v = 3:1)	Visible light 300 W Xe lamp 420 nm	Closed gas system T = 20 °C Time = 3 h	109 µmol g^{-1} h^{-1}	110
NiSe$_2$/MIL-53(Fe)	50 mg catalyst 90 mL H$_2$O 10 mL lactic acid	Visible light 300 W Xe lamp 420 nm	Quartz reactor Vol. = 250 mL T = 20 °C	10.31 mmol g^{-1} h^{-1}	111
CdLa$_2$S$_4$/MIL-88A(Fe)	50 mg catalyst 90 mL H$_2$O 10 mL ethanedioic acid	Visible light 300 W Xe lamp 420 nm	Quartz reactor Vol. = 100 mL T = 20 °C	7677.5 µmol g^{-1} h^{-1}	112
ZIS@Ni−Fe LDH	20 mg catalyst 50 mL (9:1, H$_2$O/TEOA)	Visible light 300 W Xe lamp 420 nm	Pyrex glass reactor Vol. = 120 mL	2035.81 µmol g^{-1} h^{-1}	113

14 of 20

R.R.Ikreedeegh
Russ. Chem. Rev., 2022, **91** (12) RCR5064

3.3. Photocatalytic CO_2 reduction

The conversion of CO_2 into valuable fuels and chemicals through the utilization of solar energy is considered one of the best strategies to solve the problems of global warming and fossil fuel depletion. Many attempts were performed to achieve this goal by employing various photocatalyst materials; however, a high BET surface area, available active sites and an appropriate porous structure are required for efficient sunlight-driven photocatalytic performance for CO_2 reduction. Among all other semiconductors, metal-organic frameworks (in particular, Fe-based MOFs) can provide all these properties in addition to high stability, high capacity for both CO_2 adsorption and visible light harvesting.[114]

Thermodynamically, the CO_2 gas is an extremely stable material and most of the tested pure MOFs, including Fe-containing ones, still show low activity for CO_2 reduction. Moreover, the obtained products were almost limited to formate ($HCOO^-$). Therefore, many strategies such as amine functionalization, dye sensitization and metal/non-metal doping can be applied to resolve these issues.[115] From

this point of view, the photocatalytic CO_2 reduction performance of a series of earth-abundant Fe-containing MOFs(MIL-53(Fe), MIL-101(Fe) and MIL-88B(Fe)) was investigated by Wang *et al.*[65] Due to the direct excitation of the Fe−O clusters, which promoted the electron transfer, all tested Fe-based MOFs displayed a moderate photocatalytic activity for the reduction of CO_2 into formate under visible light irradiation. The effect of amino-functionalization on these Fe-containing MOFs was further studied. Compared to non-functionalized MOFs, all amino-functionalized derivatives exhibited increased photocatalytic performance for CO_2 reduction as illustrated in Table 4. This can be attributed to the dual excitation pathways created on the NH_2 functionality and Fe−O clusters.

A significant photocatalytic CO production of 1128 µmol g^{-1} h^{-1} was also achieved under visible light irradiation by using a $[Ru(bpy)]_3^{2+}$ dye-sensitized Fe-MNS (MOF nanosheets) system.[116] The CO production was further improved to 1367 µmol g^{-1} h^{-1} with Co-doping by constructing an efficient dye/Co-Fe-MNS photocatalytic system. The $[Ru(bpy)]_3^{2+}$ dye sensitizer resulted in a negative

Table 4. Recent developments of Fe-MOFs and Fe-MOF composites for photocatalytic CO_2 reduction.

Photocatalyst	Feed composition	Light source Power Wavelength Intensity	Reactor Parameters	Product(s) Production rate	Ref.
NH_2-MIL-101(Fe)	50 mg catalyst 60 mL (5 : 1 MeCN−TEOA)	Visible light 300 W Xe lamp 420 nm	Pyrex flask Time = 8 h	$HCOO^-$ 445 µmol g^{-1} h^{-1}	65
MIL-101(Fe)	50 mg catalyst 60 mL (5 : 1 MeCN−TEOA)	Visible light 300 W Xe lamp 420 nm	Pyrex flask Time = 8 h	$HCOO^-$ 147.5 µmol g^{-1} h^{-1}	65
NH_2-MIL-53(Fe)	50 mg catalyst 60 mL (5 : 1 MeCN−TEOA)	Visible light 300 W Xe lamp 420 nm	Pyrex flask Time = 8 h	$HCOO^-$ 116.25 µmol g^{-1} h^{-1}	65
MIL-53(Fe)	50 mg catalyst 60 mL (5 : 1 MeCN−TEOA)	Visible light 300 W Xe lamp 420 nm	Pyrex flask Time = 8 h	$HCOO^-$ 74.25 µmol g^{-1} h^{-1}	65
NH_2-MIL-88(Fe)	50 mg catalyst 60 mL (5 : 1 MeCN−TEOA)	Visible light 300 W Xe lamp 420 nm	Pyrex flask Time = 8 h	$HCOO^-$ 75 µmol g^{-1} h^{-1}	65
MIL-88(Fe)	50 mg catalyst 60 mL (5 : 1 MeCN−TEOA)	Visible light 300 W Xe lamp 420 nm	Pyrex flask Time = 8 h	$HCOO^-$ 22.5 µmol g^{-1} h^{-1}	65
$MAPbI_3$@PCN-221($Fe_{0.2}$)	Catalyst CO_2 gas Ethyl acetate + H_2O	Visible light 300 W Xe lamp 400 nm	−	CO = 530 µmol g^{-1} CH_4 = 10293 µmol g^{-1}	64
$[Ru(bpy)]_3^{2+}$/Co-Fe-MNS	5 mg catalyst 5 mL acetonitrile 1 mL TEOA 20 mg $[Ru(bpy)]^{2+}$	Visible light 300 W Xe lamp 420 nm 100 mW cm^{-2}	Pyrex cell $T = 20$ °C	CO 1367 µmol g^{-1} h^{-1}	116
$[Ru(bpy)]_3^{2+}$/Fe-MNS	5 mg catalyst 5 mL acetonitrile 1 mL TEOA 20 mg $[Ru(bpy)]^{2+}$	Visible light 300 W Xe lamp 420 nm 100 mW cm^{-2}	Pyrex cell $T = 20$ °C	CO 1128 µmol g^{-1} h^{-1}	116
$CsPbBr_3$/MIL-100(Fe)	20 mg catalyst CO_2 gas H_2O vapour	Visible light 300 W Xe lamp 420 nm	Homemade Pyrex reactor Vol. = 150 mL Press. = 1 bar $T = 25$ °C	CO 20.4 µmol g^{-1} h^{-1}	117

R.R.Ikreedeegh
Russ. Chem. Rev., 2022, **91** (12) RCR5064

15 of 20

Table 4 (continued).

Photocatalyst	Feed composition	Light source Power Wavelength Intensity	Reactor Parameters	Product(s) Production rate	Ref.
MIL-100(Fe)	20 mg catalyst CO_2 gas H_2O vapour	Visible light 300 W Xe lamp 420 nm	Homemade Pyrex reactor Vol. = 150 mL Press. = 1 bar T = 20 °C	CO 4.5 µmol g^{-1} h^{-1}	117
Fe@C	catalyst $CO_2 + H_2 (1:1)$	Visible light 300 W Xe lamp	Fixed-bed reactor Time = 2 h	CO = 750 µmol g^{-1} h^{-1} CH$_4$ = 50 µmol g^{-1} h^{-1}	118
Fe-TCPP@NU-1000	3 mg catalyst CO_2 gas 0.5 mL TEOA	UV light LED lamp 390 nm 500 mW cm^{-2}	Microwave vial Vol. = 30 mL Time = 3 h	CO = 1177.8 µmol g^{-1} h^{-1} H_2 = 1077.8 µmol g^{-1} h^{-1}	119

Note. Fe-TCPP is tetra(4-carboxyphenyl)porphyrin iron(III) chloride, NU is Northwestern University (MOF).

shift of the Fe-MOF LUMO potential to fit for the theoretical thermodynamic reduction potential of CO_2/CO, while the Co doping regulated the MOF electronic structure.

In a recent study by Cheng *et al.*,[117] the Fe-based MIL-100(Fe) MOF was used to improve the CO_2 photo-reduction activity of a cesium lead bromide (CsPbBr$_3$) perovskite composite by enhancing the visible light harvest-ing and increasing the specific surface area, which is beneficial for the adsorption of CO_2 molecules. The CsPbBr$_3$/MIL-100(Fe) nanocomposites showed signifi-cantly higher activity with a CO production of 20.4 µmol g^{-1} h^{-1}, which is about five times higher com-pared to the pure CsPbBr$_3$ and MIL-100(Fe) materials. As shown in Fig. 13 *a*, a type-II heterojunction is formed, in which photoinduced electrons in the CB of CsPbBr$_3$ migrate
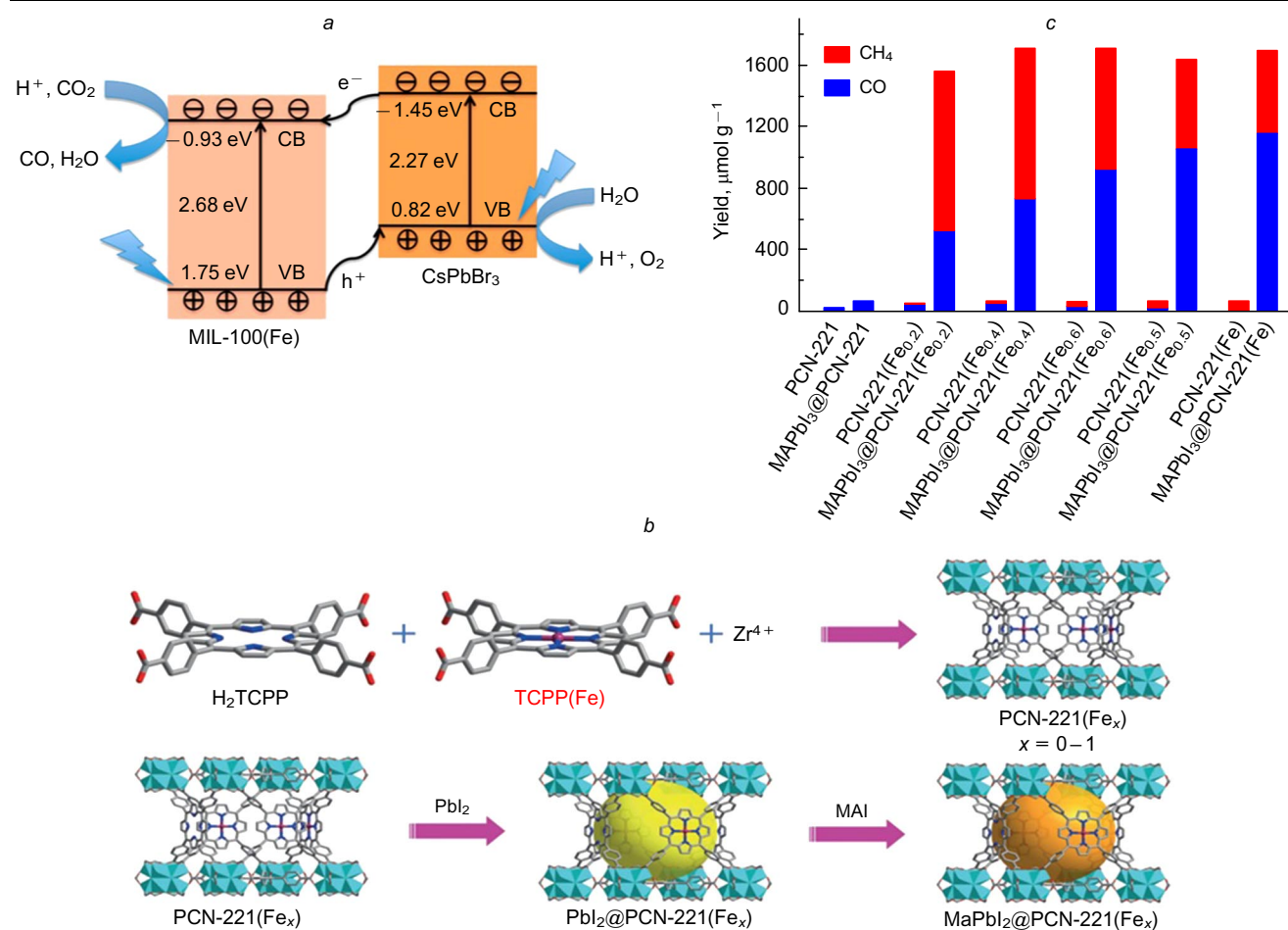
Figure 13. Proposed reaction mechanism for the CO_2 reduction over the CsPbBr$_3$/MIL-100(Fe) nanocomposite (*a*).[117] The encapsulation procedure of MAPbI$_3$ QDs in the PCN-221(Fe$_x$) MOF (*b*), amounts of CO and CH$_4$ produced over PCN-221(Fe$_x$) and MAPbI$_3$@PCN-221(Fe$_x$) in 80 h (*c*). MAI = MeNH$_3$I. Reproduced from Ref. 64 with permission from Wiley.

to the MIL-100(Fe) conduction band to reduce CO_2 gas to CO *via* a series of redox reactions, while the holes generated in the VB of MIL-100(Fe) are transferred to the VB of $CsPbBr_3$ to oxidize water.

An iron MOF-derived nanocomposite was fabricated by heating the MIL-101(Fe) MOF in a two-step calcination process.[118] The resulting Fe@C hybrid displayed a photocatalytic CO_2 conversion into CO and CH_4 of about 750 and 50 μmol, respectively, after 2 h of light irradiation. However, extremely good results were reported by using a photothermal approach, in which both photocatalytic and thermocatalytic CO_2 reductions are combined in one system. This extra enhancement was attributed to the thermal effect caused by the intense absorption of visible light and infrared radiation.

Iron-containing MOFs can also be used to increase the stability of other photocatalyst materials in aqueous reaction systems as investigated recently by Wu *et al.*,[64] who encapsulated a low-cost perovskite of methyl ammonium lead iodide ($MeNH_3PbI_3$), abbreviated as $MAPbI_3$, into Fe-porphyrin-based MOF (PCN-221(Fe)) and tested the resulting composite for photocatalytic CO_2 reduction. The encapsulation process was carried out stepwise as depicted in Fig. 13 *b*. Firstly, the $PCN\text{-}221(Fe_x)$ MOF was synthesized with various Fe contents. The prepared samples were immersed in PbI_2 and MAI ethanol solutions, respectively, to encapsulate the $MAPbI_3$ quantum dots (QDs) in the MOF pores. The composite photocatalyst exhibited exceptional photocatalytic activity with CO and CH_4 productions of 530 and 10293 μmol g^{-1}, respectively. This enhancement was attributed to both improved stability and Fe catalytic sites, which increased the transfer of photogenerated electrons (Fig. 13 *c*).

3.4. Photodegradation of pollutants

Metal-organic frameworks, particularly Fe-based MOFs, and their composites have been widely used for photocatalytic degradation of organic pollutants and related environmental applications. Iron-based MOFs are extremely attractive since they show strong absorption of visible light due to the existence of numerous iron-oxo (Fe−O) clusters that make them good Fenton-like catalysts.[120] They also have strong coordination bonds, impacting high chemical and water resistance to such MOFs.[121]

When light strikes the surface of these Fe-based MOFs, they generate electrons in the valence band, which then move to the conduction band, leaving holes in the VB. Due to the strong reducing power of these photogenerated electrons, they reduce Fe(III) to Fe(II), which then react to produce a large amount of free radicals (*e.g.*, $^\bullet OH$) that can decompose organic pollutants.[47, 115, 122]

Despite these advances in the field of photocatalysis, pristine Fe-based MOFs still have a problem with rapid recombination of photogenerated electron-hole pairs leading to low photocatalytic activity. To overcome this issue, many strategies can be applied including bandgap engineering through electron-donating or withdrawing species (*e.g.*, $-NH_2$, $-OH$ or $-COOH$),[123, 124] modifying these pristine Fe-MOFs by introducing metal/non-metals or semiconductor nanoparticles to form efficient heterojunctions,[125, 126] introducing sacrificial agents and electron acceptors using H_2O_2.[127]

In recent years, Guo *et al.*[128] prepared a Fe-based MOF-derived composite and tested it for photocatalytic degradation of tetracycline, which is considered one of the most commonly used antibiotics, under visible light irradiation. A Fe-MOF-derived composite was synthesized through a co-calcination of melamine and MIL-53(Fe) MOF to obtain a Z-scheme heterojunction photocatalyst named $\alpha\text{-}Fe_2O_3@g\text{-}C_3N_4$. The resulting $\alpha\text{-}Fe_2O_3$ nanoparticles had a smaller particle size than spindle-shaped MIL-53(Fe) as seen from the SEM images in Fig. 14 *a* and *b*. This might be attributed to the partial collapse in the MIL-53(Fe) inner structure caused by the calcination process. As depicted in Fig. 14 *c*, the new photocatalyst composite promoted the degradation of ~92% of tetracycline with the highest degradation rate of 0.042 min^{-1}, which is 6, 7 and 14 times higher than those using pure MIL-53(Fe), $\alpha\text{-}Fe_2O_3$ and $g\text{-}C_3N_4$, respectively.

Three Fe-based MOFs (MIL-100(Fe), MIL-101(Fe) and Fe-MIL-53(Fe)) were also tested for photocatalytic degradation of tetracycline under visible light irradiation.[120] The
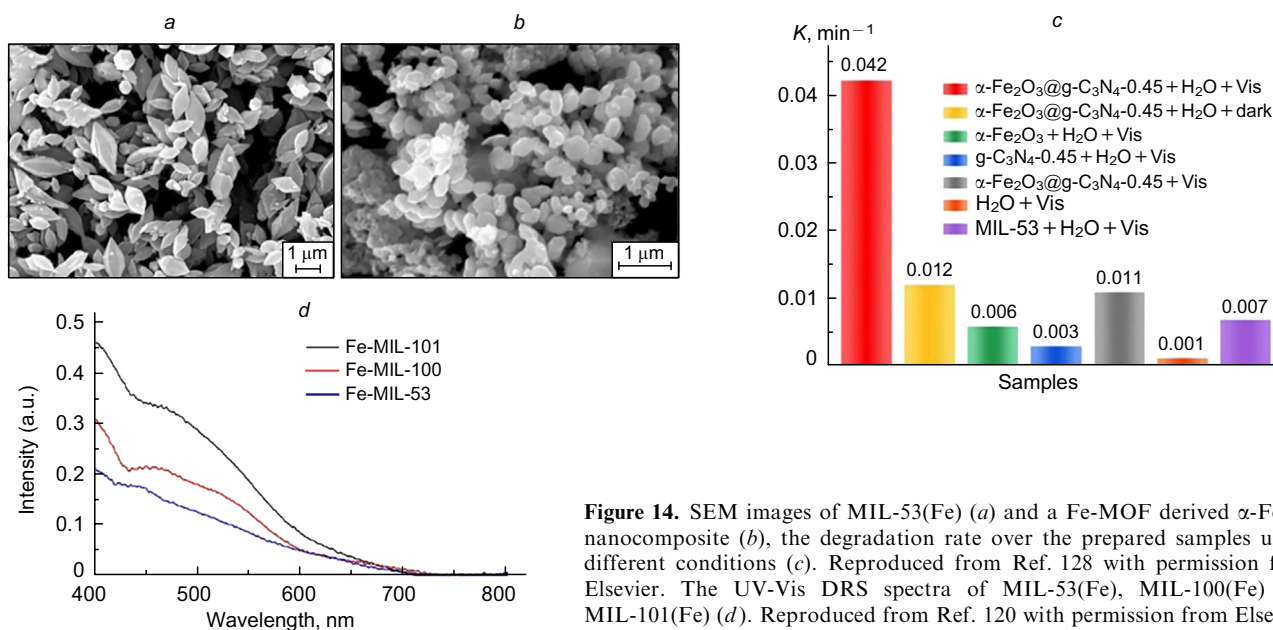
Figure 14. SEM images of MIL-53(Fe) (*a*) and a Fe-MOF derived $\alpha\text{-}Fe_2O_3$ nanocomposite (*b*), the degradation rate over the prepared samples under different conditions (*c*). Reproduced from Ref. 128 with permission from Elsevier. The UV-Vis DRS spectra of MIL-53(Fe), MIL-100(Fe) and MIL-101(Fe) (*d*). Reproduced from Ref. 120 with permission from Elsevier.

R.R.Ikreedeegh
Russ. Chem. Rev., 2022, **91** (12) RCR5064

17 of 20

highest tetracycline removal performance (96.6%) was observed using the MIL-101(Fe) MOF compared to 57.4% and 40.6% for MIL-100(Fe) and MIL-53(Fe), respectively. This large difference in the photodegradation performance may be due to higher visible-light harvesting attained by the Fe-MIL-101(Fe) MOF as shown in Fig. 14 *d*. Moreover, the Fe-MIL-101(Fe) MOF had the maximum adsorption rate since it exhibited the highest pore volume and the largest pore size (0.86 cm^3 g^{-1} and 25.74 nm, respectively) compared to MIL-100(Fe) (0.34 cm^3 g^{-1} and 2.27 nm) and MIL-53(Fe) (0.04 cm^3 g^{-1} and 4.6 nm).

In 2021, Zhang and Guo [129] reported the synthesis of a novel Fe-based MOF (Fe-BDC, BDC is benzenedicarboxylate) and a CdSe QDs nanocomposite (CdSe@Fe-BDC) for photocatalytic degradation of rhodamine B (RhB) dye under visible light irradiation. Compared to the pristine Fe-BDC MOF, the CdSe@Fe-BDC photocatalyst exhibited a degradation rate of 99.8% which is 5.8 times higher due to the interfacial contact and the formed heterostructure, thereby promoting the electron transfer from CdSe to MOF and significantly facilitating the separation of photogenerated electron-hole pairs.

In addition to the photodegradation of organic pollutants in aqueous phases, Fe-based MOFs were also applied for photocatalytic reduction of heavy metal ions such as Cr(VI), which is considered to be one of the toxic wastewater pollutants. One of the most effective strategies to remove this pollutant from wastewater is the reduction of Cr(VI) to Cr(III).[130] Wu and co-authors[131] investigated the use of the MIL-53(Fe) MOF for the photocatalytic degradation of Cr(VI) under visible light irradiation. The photocatalyst displayed an exceptional photocatalytic performance with a reduction rate of 100% within 40 min. Moreover, by using a Cr(VI)-dye solution, a photocatalytic Cr(VI) reduction of 60% and photocatalytic dye degradation of 80% were achieved, revealing that the MIL-53(Fe) MOF can act as a bifunctional oxidation/reduction photocatalyst for environmental applications. The recent advances of Fe-based MOFs and their composites for photocatalytic degradation of different pollutants are summarized in Table 5.

Table 5. Recent developments of Fe-MOFs and Fe-MOF composites for photocatalytic degradation of pollutants.

Photocatalyst	Application	Feed composition	Light source Power Wavelength Intensity	Reactor Parameters	Conversion (%)	Ref.
MIL-101(Fe)	Degradation of tetracycline (TC)	50 mg catalyst 50 mg TC 100 mL H_2O	Visible light 300 W Xe lamp 420 nm	Pyrex cell Time = 3 h	96.6	120
MIL-100(Fe)	Degradation of TC	50 mg catalyst 50 mg TC 100 mL H_2O	Visible light 300 W Xe lamp 420 nm	Pyrex cell Time = 3 h	57.4	120
MIL-53(Fe)	Degradation of TC	50 mg catalyst 50 mg TC 100 mL H_2O	Visible light 300 W Xe lamp 420 nm	Pyrex cell Time = 3 h	40.6	120
α-Fe_2O_3@g-C_3N_4	Degradation of TC	0.05 g catalyst 100 mL TC sol. (40 mgL^{-1})	Visible light 100W LED lamp 420 nm	Glass reactor T = 25 °C Vol. = 250 mL pH 5.5	92	128
CdSe@Fe-BDC	Degradation of RhB	50 mg catalyst 100 mL RhB sol. (50 ppm)	Visible light 250W Na lamp 555 nm	Glass beaker Vol. = 250 mL Time = 4 h	99.8	129
MIL-53(Fe)	Degradation of Cr(VI)	40 mg catalyst 40 mL Cr(VI) sol. (20 ppm)	Visible light 300 W Xe lamp 420 nm	Quartz reactor T = 30 °C Vol. = 100 mL Time = 40 min pH 4	100	130
MIL-53(Fe)/$MoSe_2$	Degradation of RhB	10 mg catalyst 20 mL RhB sol. (100 mgL^{-1})	UV-vis light 300 W Xe lamp 554 nm	Quartz cuvette	98.83	132
MIL-53(Fe)/$MoSe_2$	Degradation of TC	10 mg catalyst 20 mL RhB sol. (100 mgL^{-1})	UV-vis light 300 W Xe lamp 357 nm	Quartz cuvette	99.00	132
MIL-53(Fe)/Bi_2WO_6	Degradation of RhB	100 mg catalyst RhB sol. (20 mgL^{-1})	Visible light 420 nm	Time = 80 min	80.00	133
Fe_2O_4@MIL-53(Fe)	Degradation of IBP	20 mg catalyst 50 mL IBP sol. (10 mgL^{-1}) H_2O_2	Visible light 500 W Xe lamp 420 nm	Batch reactor Time = 60 min	99.00	134
Fe-MOF@BiOBr/ M−CN	Degradation of ciprofloxacin (CIP)	catalyst CIP solution	Visible light	Time = 120 min	93.00	135

18 of 20

R.R.Ikreedeegh
Russ. Chem. Rev., 2022, **91** (12) RCR5064

4. Conclusion

Recently, the photocatalysis process has gained great attention as one of the best strategies to solve the problem of energy shortage and environmental crisis using four main photocatalytic applications such as H_2 production, O_2 production, CO_2 reduction and photodegradation of pollutants. Currently, metal-organic framework materials, in particular, Fe-based MOFs, are presented as successfully used photocatalysts in these fields. In this review, six main synthetic approaches to Fe-based MOFs are considered and explained in detail. Among these approaches, the solvothermal synthesis was primarily used; however, the microwave and sonochemical techniques are gaining more priority as being fast and energy-efficient. Some unconventional techniques such as electrochemical and mechanochemical methods can be used for industrial scale-up production. Minimum waste disposal, continuous production with controlled shape and structure of the resulting Fe-based MOFs can be achieved using a dry-gel method.

This review also summarizes the recent advances in the use of Fe-based MOFs for the aforementioned photocatalytic applications. Iron-based MOFs, Fe-MOF composites and nanostructured materials derived there from showed excellent performance. It can be concluded that the yields of photocatalytic production are greatly affected by many factors including operating parameters, morphological properties, Fe-based MOF functionalization, surface area and porosity. However, Fe-based MOF photocatalysts still have some limitations and issues, for which the following recommendations should be considered in the future:

— More research is needed to gain insight into the possibility of combining various conventional and non-conventional methods for the synthesis of Fe-based MOF to improve physical, chemical and electrical properties.

— Pure Fe-based MOF photocatalysts showed poor results compared to their composites; therefore, greater emphasis should be given to the preparation of Fe-based MOFs with other materials such as perovskite, LDH and metal oxide nanocomposites.

— Some of the reported Fe-based MOFs showed relatively poor stability in reactions involving water; hence, the development of more reliable MOF photocatalysts in water medium is highly essential.

— More attention needs to be paid to understanding the photocatalytic reaction mechanisms and the resulting heterojunctions such as Z- and S-schemes of Fe-based MOF composites.

— Research into photocatalytic applications involving biologically active and radioactive pollutants is very rare; hence, the use of Fe-based MOF photocatalysts for these purposes should be considered.

5. List of acronyms

BDC — benzenedicarboxylate (ligand),
BET — Brunauer–Emmett–Teller (theory),
bpy — 2,2′-bipyridine,
BTC — benzenetricarboxylic (MOF),
CB — conduction band,
CIP — ciprofloxacin (dye),
CNT — carbon nanotube,
DGC — dry-gel conversion,
DEF — diethylformamide,
DMA — dimethylacetamide,
DMF — dimethylformamide,
DRS — diffuse reflectance spectroscopy,
EY — Eosin Y (dye),
g-C_3N_4 — graphitic carbon nitride,
GHG — greenhouse gas,
GO — graphene oxide,
h^+ — hole,
HOMO — highest occupied molecular orbital,
IBP — ibuprofen (dye),
LAG — liquid-assisted grinding,
LDH — layered double hydroxides,
LUMO — lowest unoccupied molecular orbital,
$MAPbI_3$ — $MeNH_3PbI_3$,
MIL — Materials Institute Lavoisier (MOF),
MNS — MOF nanosheet,
MOF — metal-organic framework,
MTBS — tributylmethylammonium methyl sulfate,
NC — nanocomposite,
NG — neat grinding,
NNU — Northeast Normal University,
NP — nanoparticle,
NU — Northwestern University (MOF),
OER — oxygen evolution reactions,
PC — photocatalyst,
PCN — porous coordination network (MOF),
PL — photoluminescence (spectrum),
POM — polyoxometalate (anions),
QD — quantum dots,
RhB — rhodamine B (dye),
SAG — steam-assisted conversion,
SEM — scanning electron microscopy,
TC — tetracycline (dye),
TEOA — triethanolamine,
TMAOH — tetramethylammonium hydroxide,
UiO — Universiteteti Oslo (MOF),
UV — ultraviolet,
VB — valence band,
ZIF — zeolitic imidazolate frameworks (MOFs).

6. References

1. B.Huskinson, M.P.Marshak, C.Suh, S.Er, M.R.Gerhardt, C.J.Galvin, X.Chen, A.Aspuru-Guzik, R.G.Gordon, M.J.Aziz. *Nature (London)*, **505**, 195 (2014)
2. F.V.Bekun, A.A.Alola, S.A.Sarkodie. *Sci. Total Environ.*, **657**, 1023 (2019)
3. A.Goeppert, M.Czaun, J.-P.Jones, G.S.Prakash, G.A.Olah. *Chem. Soc. Rev.*, **43**, 7995 (2014)
4. M.Tahir, N.S.Amin. *Energy Convers. Manage.*, **76**, 194 (2013)
5. K.Kabra, R.Chaudhary, R.L.Sawhney. *Ind. Eng. Chem. Res.*, **43**, 7683 (2004)
6. A.Fujishima, K.Honda. *Nature (London)*, **238**, 37 (1972)
7. M.Madi, M.Tahir. *Mater. Sci. Semicond. Proc.*, **142**, 106517 (2022)
8. W.K.Fan, M.Tahir. *Energy Convers. Manag.*, **254**, 115240 (2022)
9. T.Kamegawa, Y.Ishiguro, R.Kido, H.Yamashita. *Molecules*, **19**, 16477 (2014)
10. P.F.Lim, K.H.Leong, L.C.Sim, W.-D.Oh, Y.H.Chin, P.Saravanan, C.Dai. *Appl. Phys. A*, **126**, 1 (2020)
11. G.Williams, B.Seger, P.V.Kamat. *ACS Nano*, **2**, 1487 (2008)
12. M.-Q.Yang, N.Zhang, Y.-J.Xu. *ACS Appl. Mater. Interfaces*, **5**, 1156 (2013)
13. Y.Zhou, R.Abazari, J.Chen, M.Tahir, A.Kumar, R.R.Ikreedeegh, E.Rani, H.Singh, A.M.Kirillov. *Coord. Chem. Rev.*, **451**, 214264 (2022)

R.R.Ikreedeegh
Russ. Chem. Rev., 2022, **91** (12) RCR5064

19 of 20

14. A.Kuznetsova, V.Matveevskaya, D.Pavlov, A.Yakunenkov, A.Potapov. *Materials*, **13**, 2699 (2020)

15. X.Luo, R.Abazari, M.Tahir, W.K.Fan, A.Kumar, T.Kalhorizadeh, A.M.Kirillov, A.R.Amani-Ghadim, J.Chen, Y.Zhou. *Coord. Chem. Rev.*, **461**, 214505 (2022)

16. J.Chen, R.Abazari, K.A.Adegoke, N.W.Maxakato, O.S.Bello, M.Tahir, S.Tasleem, S.Sanati, A.M.Kirillov, Y.Zhou. *Coord. Chem. Rev.*, **469**, 214664 (2022)

17. S.Tasleem, M.Tahir, W.A.Khalifa. *Int. J.Hydrogen Energy*, **46**, 14148 (2021)

18. R.Ning, H.Pang, Z.Yan, Z.Lu, Q.Wang, Z.Wu, W.Dai, L.Liu, Z.Li, G.Fan. *J. Hazard. Mater.*, **435**, 129061 (2022)

19. Z.Guan, S.Zhu, S.Ding, D.Xia, D.Li. *Chemosphere*, **299**, 134481 (2022)

20. Q.Xia, H.Wang, B.Huang, X.Yuan, J.Zhang, J.Zhang, L.Jiang, T.Xiong, G.Zeng. *Small*, **15**, 1803088 (2019)

21. M.Alvaro, E.Carbonell, B.Ferrer, F.X.Llabrés i Xamena, H.Garcia. *Chem. – Eur. J.*, **13**, 5106 (2007)

22. L.Shen, R.Liang, M.Luo, F.Jing, L.Wu. *Phys. Chem. Chem. Phys.*, **17**, 117 (2015)

23. J.X.Liu, M.Y.Gao, W.H.Fang, L.Zhang, J.Zhang. *Angew. Chem.*, **128**, 5246 (2016)

24. J.Joseph, S.Iftekhar, V.Srivastava, Z.Fallah, E.N.Zare, M.Sillanpää. *Chemosphere*, **284**, 131171 (2021)

25. D.Wang, Z.Li. *Res. Chem. Intermed.*, **43**, 5169 (2017)

26. S.Yuan, L.Feng, K.Wang, J.Pang, M.Bosch, C.Lollar, Y.Sun, J.Qin, X.Yang, P.Zhang. *Adv. Mater.*, **30**, 1704303 (2018)

27. D.Feng, W.-C.Chung, Z.Wei, Z.-Y.Gu, H.-L.Jiang, Y.-P.Chen, D.J.Darensbourg, H.-C.Zhou. *J.Am. Chem. Soc.*, **135**, 17105 (2013)

28. A.Henschel, K.Gedrich, R.Kraehnert, S.Kaskel. *Chem. Commun.*, 4192 (2008)

29. P.Horcajada, S.Surblé, C.Serre, D.-Y.Hong, Y.-K.Seo, J.-S.Chang, J.-M.Grenèche, I.Margiolaki, G.Férey. *Chem. Commun.*, 2820 (2007)

30. A.Artem'ev, V.Fedin. *Russ. J. Org. Chem.*, **55**, 800 (2019)

31. A.Dhakshinamoorthy, M.Alvaro, H.Chevreau, P.Horcajada, T.Devic, C.Serre, H.Garcia. *Catal. Sci.Technol.*, **2**, 324 (2012)

32. H.Li, M.Eddaoudi, M.O'Keeffe, O.M.Yaghi. *Nature (London)*, **402**, 276 (1999)

33. R.-B.Lin, S.Xiang, H.Xing, W.Zhou, B.Chen. *Coord. Chem. Rev.*, **378**, 87 (2019)

34. O.M.Yaghi, G.Li, H.Li. *Nature (London)*, **378**, 703 (1995)

35. W.Zhang, W.Huang, J.Jin, Y.Gan, S.Zhang. *Appl. Catal., B: Environmental*, **292**, 120197 (2021)

36. W.Huang, X.Wang, W.Zhang, S.Zhang, Y.Tian, Z.Chen, W.Fang, J.Ma. *Appl. Catal., B: Environmental*, **273**, 119087 (2020)

37. Y.Shi, A.-F.Yang, C.-S.Cao, B.Zhao. *Coord. Chem. Rev.*, **390**, 50 (2019)

38. S.Wang, W.Yao, J.Lin, Z.Ding, X.Wang. *Angew. Chem., Int. Ed.*, **53**, 1034 (2014)

39. S.Yan, S.Ouyang, H.Xu, M.Zhao, X.Zhang, J.Ye. *J. Mater. Chem. A*, **4**, 15126 (2016)

40. X.Zhang, J.Wang, X.-X.Dong, Y.-K.Lv. *Chemosphere*, **242**, 125144 (2020)

41. L.Shen, R.Liang, L.Wu. *Chin. J. Chem*, **36**, 2071 (2015)

42. R.R.Ikreedeegh, M.Tahir. *J. Environ. Chem. Eng.*, 105600 (2021)

43. R.R.Ikreedeegh, M.Tahir. *Fuel*, **305**, 121558 (2021)

44. X.Zhao, Z.Lu, Y.Zhang, M.Zhou, S.Xu, Z.Li. *J. Mater. Sci: Mater. Electron.*, 1 (2022)

45. J.Gu, H.Fan, C.Li, J.Caro, H.Meng. *Angew. Chem.*, **131**, 5351 (2019)

46. Y.Lee, S.Kim, H.Fei, J.K.Kang, S.M.Cohen. *Chem. Commun.*, **51**, 16549 (2015)

47. R.R.Ikreedeegh, M.Tahir. *J.CO$_2$ Util.*, **43**, 101381 (2021)

48. J.-R.Li, Y.Ma, M.C.McCarthy, J.Sculley, J.Yu, H.-K.Jeong, P.B.Balbuena, H.-C.Zhou. *Coord. Chem. Rev.*, **255**, 1791 (2011)

49. H.Zhang, G.Zhai, L.Lei, C.Zhang, Y.Liu, Z.Wang, H.Cheng, Z.Zheng, P.Wang, Y.Dai. *J. Colloid Interface Sci.*, **625**, 33 (2022)

50. Y.Qin, S.Yang, X.You, Y.Liu, L.Qin, Y.Li, W.Zhang, W.Liang. *Sep. Purif. Technol.*, 121325 (2022)

51. K.G.Laurier, F.Vermoortele, R.Ameloot, D.E.De Vos, J.Hofkens, M.B.Roeffaers. *J. Am. Chem. Soc.*, **135**, 14488 (2013)

52. Y.Li, Z.Dong, L.Jiao. *Adv. Energy Mater.*, **10**, 1902104 (2020)

53. H.Liu, M.Zha, Z.Liu, J.Tian, G.Hu, L.Feng. *Chem. Commun.*, **56**, 7889 (2020)

54. M.Yang, Y.-N. Zhou, Y.-N. Cao, Z.Tong, B.Dong, Y.-M.Chai. *Appl. Mater. Today*, **20**, 100692 (2020)

55. J.Liu, X.Zhao, P.Jing, W.Shi, P.Cheng. *Chem. – Eur. J.*, **25**, 2330 (2019)

56. X.Zhao, P.Pachfule, S.Li, J.R.J.Simke, J.Schmidt, A.Thomas. *Angew. Chem.*, **130**, 9059 (2018)

57. E.N. Augustus, A.Nimibofa, I.A.Kesiye, W.Donbebe. *Am. J. Environ. Prot.*, **5**, 61 (2017)

58. W.K.Fan, M.Tahir. *Energy Convers. Manag.*, **253**, 115180 (2022)

59. C.Dey, T.Kundu, B.P.Biswal, A.Mallick, R.Banerjee. *Acta Crystallogr., Sect. B: Struct. Sci. Cryst. Eng. Mater.*, **70**, 3 (2014)

60. T.R.Whitfield, X.Wang, L.Liu, A.J.Jacobson. *Solid State Sciences*, **7**, 1096 (2005)

61. D.Feng, K.Wang, Z.Wei, Y.-P.Chen, C.M.Simon, R.K.Arvapally, R.L.Martin, M.Bosch, T.-F.Liu, S.Fordham. *Nat. Commun.*, **5**, 1 (2014)

62. S.Li, F.Wu, R.Lin, J.Wang, C.Li, Z.Li, J.Jiang, Y.Xiong. *Chem. Eng. J.*, **429**, 132217 (2022)

63. F.Dai, Y.Wang, X.Zhou, R.Zhao, J.Han, L.Wang. *Appl. Surf. Sci.*, **517**, 146161 (2020)

64. L.Y.Wu, Y.F.Mu, X.X.Guo, W.Zhang, Z.M.Zhang, M.Zhang, T.B.Lu. *Angew. Chem., Int. Ed.*, **58**, 9491 (2019)

65. D.Wang, R.Huang, W.Liu, D.Sun, Z.Li. *ACS Catal.*, **4**, 4254 (2014)

66. T.Chalati, P.Horcajada, R.Gref, P.Couvreur, C.Serre. *J. Mater. Chem.*, **21**, 2220 (2011)

67. J.Kim, S.-T.Yang, S.B.Choi, J.Sim, J.Kim, W.-S.Ahn. *J. Mater. Chem.*, **21**, 3070 (2011)

68. K.M.Taylor-Pashow, J.Della Rocca, Z.Xie, S.Tran, W.Lin. *J. Am. Chem. Soc.*, **131**, 14261 (2009)

69. W.Guo, W.Sun, L.-P.Lv, S.Kong, Y.Wang. *ACS Nano*, **11**, 4198 (2017)

70. Y.Dong, T.Hu, M.Pudukudy, H.Su, L.Jiang, S.Shan, Q.Jia. *Mater. Chem. Phys.*, **251**, 123060 (2020)

71. P.Horcajada, C.Serre, M.Vallet-Regí, M.Sebban, F.Taulelle, G.Férey. *Angew. Chem., Int. Ed.*, **118**, 6120 (2006)

72. S.H.Jhung, J.H.Lee, J.W.Yoon, C.Serre, G.Férey, J.S.Chang. *Adv. Mater.*, **19**, 121 (2007)

73. N. Campagnol, T.Van Assche, T.Boudewijns, J.Denayer, K.Binnemans, D.De Vos, J.Fransaer. *J. Mater. Chem. A*, **1**, 5827 (2013)

74. H.Pourfarzad, M.Shabani-Nooshabadi, M.R.Ganjali. *J. Power Sources*, **451**, 227768 (2020)

75. S.Achmann, G.Hagen, J.Kita, I.M.Malkowsky, C.Kiener, R.Moos. *Sensors*, **9**, 1574 (2009)

76. M.Pilloni, F.Padella, G.Ennas, S.Lai, M.Bellusci, E.Rombi, F.Sini, M.Pentimalli, C.Delitala, A.Scano. *Micropor. Mesopor. Mater.*, **213**, 14 (2015)

77. H.Jeong, J.Lee. *Eur. J. Inorg. Chem.*, **2019**, 4597 (2019)

78. D.He, H.Niu, S.He, L.Mao, Y.Cai, Y.Liang. *Water Res.*, **162**, 151 (2019)

79. B.E.Souza, A.F.Möslein, K.Titov, J.D.Taylor, S.Rudic, J.-C.Tan. *ACS Sustainable Chem. Eng.*, **8**, 8247 (2020)

80. I.Ahmed, J.Jeon, N.A.Khan, S.H.Jhung. *Cryst. Growth Design*, **12**, 5878 (2012)

81. N. Tannert, S.Gökpinar, E.Hastürk, S.Nießing, C.Janiak. *Dalt. Trans.*, **47**, 9850 (2018)

20 of 20

R.R.Ikreedeegh
Russ. Chem. Rev., 2022, **91** (12) RCR5064

82. Y.Luo, B.Tan, X.Liang, S.Wang, X.Gao, Z.Zhang, Y.Fang. *Microporous and Mesoporous Mater.*, **297**, 110034 (2020)
83. A.Gedanken. *Ultrason. Sonochem.*, **11**, 47 (2004)
84. K.S.Suslick, D.A.Hammerton, R.E.Cline. *J. Am. Chem. Soc.*, **108**, 5641 (1986)
85. K.S.Suslick, S.-B.Choe, A.A.Cichowlas, M.W.Grinstaff. *Nature (London)*, **353**, 414 (1991)
86. J.Amaro-Gahete, R.Klee, D.Esquivel, J.R.Ruiz, C.Jimenez-Sanchidrian, F.J.Romero-Salguero. *Ultrason. Sonochem.*, **50**, 59 (2019)
87. S.-E.Park, J.-S.Chang, Y.K.Hwang, D.S.Kim, S.H.Jhung, J.S.Hwang. *Catal. Surv. Asia*, **8**, 91 (2004)
88. K.Hindelang, S.I.Vagin, C.Anger, B.Rieger. *Chem. Commun.*, **48**, 2888 (2012)
89. W.Dong, X.Liu, W.Shi, Y.Huang. *Rsc Adv.*, **5**, 17451 (2015)
90. M.Pu, Z.Guan, Y.Ma, J.Wan, Y.Wang, M.L.Brusseau, H.Chi. *Appl. Catal., A: General*, **549**, 82 (2018)
91. A.Pichon, A.Lazuen-Garay, S.L.James. *CrystEngComm*, **8**, 211 (2006)
92. N.Stock, S.Biswas. *Chem. Rev.*, **112**, 933 (2012)
93. P.J.Beldon, L.Fábián, R.S.Stein, A.Thirumurugan, A.K.Cheetham, T.Friščić. *Angew. Chem., Int. Ed.*, **122**, 9834 (2010)
94. Q.Liu, Z.-X.Low, L.Li, A.Razmjou, K.Wang, J.Yao, H.Wang. *J. Mater. Chem. A*, **1**, 11563 (2013)
95. T.Friščić, I.Halasz, P.J.Beldon, A.M.Belenguer, F.Adams, S.A.Kimber, V.Honkimäki, R.E.Dinnebier. *Nat. Chem.*, **5**, 66 (2013)
96. J.-L.Do, T.Friščić. *ACS Cent. Sci.*, **3**, 13 (2017)
97. W.Xu, J.Dong, J.Li, J.Li, F.Wu. *J. Chem. Soc., Chem. Commun.*, 755 (1990)
98. A.K.Das, R.S.Vemuri, I.Kutnyakov, B.P.McGrail, R.K.Motkuri. *Sci. Reports*, **6**, 1 (2016)
99. J.Ren, X.Dyosiba, N.M.Musyoka, H.W.Langmi, M.Mathe, S.Liao. *Coord. Chem. Rev.*, **352**, 187 (2017)
100. W.A.Shah, A.Waseem, M.A.Nadeem, P.Kögerler. *Appl. Catal., A: General*, **567**, 132 (2018)
101. L.-L.Qu, J.Wang, T.-Y.Xu, Q.-Y.Chen, J.-H.Chen, C.-J.Shi. *Sustainable Energy Fuels*, **2**, 2109 (2018)
102. S.Li, J.Tan, Z.Jiang, J.Wang, Z.Li. *Chem. Eng. J.*, **384**, 123354 (2020)
103. Z.Lionet, T.-H.Kim, Y.Horiuchi, S.W.Lee, M.Matsuoka. *J. Phys. Chem. C*, **123**, 27501 (2019)
104. L.Chi, Q.Xu, X.Liang, J.Wang, X.Su. *Small*, **12**, 1351 (2016)
105. Y.Horiuchi, T.Toyao, K.Miyahara, L.Zakary, D.Do Van, Y.Kamata, T.-H.Kim, S.W.Lee, M.Matsuoka. *Chem. Commun.*, **52**, 5190 (2016)
106. M.Z.Hussain, Z.Yang, Z.Huang, Q.Jia, Y.Zhu, Y.Xia. *Adv. Sci.*, **8**, 2100625 (2021)
107. Y.Kataoka, K.Sato, Y.Miyazaki, K.Masuda, H.Tanaka, S.Naito, W.Mori. *Energy Environ. Sci.*, **2**, 397 (2009)
108. C.Gomes Silva, I.Luz, F.X.Llabres i Xamena, A.Corma, H.García. *Chem. – Eur. J.*, **16**, 11133 (2010)
109. X.Zou, Y.Zhang. *Chem. Soc. Rev.*, **44**, 5148 (2015)
110. D.Wang, Y.Song, J.Cai, L.Wu, Z.Li. *New J. Chem.*, **40**, 9170 (2016)
111. Q.Chen, J.Zhang, J.Lu, H.Liu. *Int. J. Hydrogen Energy*, **44**, 16400 (2019)
112. Q.Chen, J.Li, L.Cheng, H.Liu. *Chem. Eng. J.*, **379**, 122389 (2020)
113. S.Zhao, Q.Liang, W.Gao, M.Zhou, C.Yao, S.Xu, Z.Li. *Inorg. Chem.*, **60**, 9762 (2021)
114. I.I.Alkhatib, C.Garlisi, M.Pagliaro, K.Al-Ali, G.Palmisano. *Catal. Today*, **340**, 209 (2020)
115. R.R.Ikreedeegh, M.Tahir. *J. Mater. Sci.*, **56**, 18989 (2021)
116. A.M.Idris, X.Jiang, J.Tan, Z.Cai, X.Lou, J.Wang, Z.Li. *J. Colloid Interface Sci.*, **607**, 1180 (2022)
117. R.Cheng, E.Debroye, J.Hofkens, M.B.Roeffaers. *Catalysts*, **10**, 1352 (2020)
118. H.Zhang, T.Wang, J.Wang, H.Liu, T.D.Dao, M.Li, G.Liu, X.Meng, K.Chang, L.Shi. *Adv. Mater.*, **28**, 3703 (2016)
119. K.Zhang, S.Goswami, H.Noh, Z.Lu, T.Sheridan, J.Duan, W.Dong, J.T.Hupp. *J. Photochem. Photobiol.*, **10**, 100111 (2022)
120. D.Wang, F.Jia, H.Wang, F.Chen, Y.Fang, W.Dong, G.Zeng, X.Li, Q.Yang, X.Yuan. *J. Colloid Interface Sci.*, **519**, 273 (2018)
121. R.Liang, R.Chen, F.Jing, N. Qin, L.Wu. *Dalton Trans.*, **44**, 18227 (2015)
122. G.Férey, C.Mellot-Draznieks, C.Serre, F.Millange, J.Dutour, S.Surblé, I.Margiolaki. *Science*, **309**, 2040 (2005)
123. L.Shi, T.Wang, H.Zhang, K.Chang, X.Meng, H.Liu, J.Ye. *Adv. Sci.*, **2**, 1500006 (2015)
124. S.Li, S.Sun, H.Wu, C.Wei, Y.Hu. *Catal. Sci. Technol.*, **8**, 1696 (2018)
125. J.Qiu, X.Zhang, Y.Feng, X.Zhang, H.Wang, J.Yao. *Appl. Catal., B: Environmental*, **231**, 317 (2018)
126. M.Wen, K.Mori, Y.Kuwahara, H.Yamashita. *ACS Energy Lett.*, **2**, 1 (2017)
127. X.Li, Y.Pi, L.Wu, Q.Xia, J.Wu, Z.Li, J.Xiao. *Appl. Catal., B: Environmental*, **202**, 653 (2017)
128. T.Guo, K.Wang, G.Zhang, X.Wu. *Appl. Surf. Sci.*, **469**, 331 (2019)
129. Y.Zhang, G.Li, Q.Guo. *Micropor. Mesopor. Mater.*, **324**, 111291 (2021)
130. J.-C.Wang, J.Ren, H.-C.Yao, L.Zhang, J.-S.Wang, S.-Q.Zang, L.-F.Han, Z.-J.Li. *J. Hazard. Mater.*, **311**, 11 (2016)
131. R.Liang, F.Jing, L.Shen, N. Qin, L.Wu. *J. Hazard. Mater.*, **287**, 364 (2015)
132. X.Guo, D.Yin. *Ionics*, 1 (2022)
133. Y.Tu, L.Ling, Q.Li, X.Long, N. Liu, Z.Li. *Opt. Mater.*, **110**, 110500 (2020)
134. N. Liu, J.Wang, J.Wu, Z.Li, W.Huang, Y.Zheng, J.Lei, X.Zhang, L.Tang. *Mater. Res. Bull.*, **132**, 111000 (2020)
135. Y.Pan, X.Hu, D.Shen, Z.Li, R.Chen, Y.Li, J.Lu, M.Bao. *Sep. Purif. Technol.*, **295**, 121216 (2022)